1   FORWARD GEOCHEMICAL MODELING AS A GUIDING TOOL DURING

2   EXPLORATION OF SEA CLIFF HYDROTHERMAL FIELD, GORDA RIDGE

3   Vincent Milesi[1,*], Everett Shock[1,2], Tucker Ely[1] , Megan Lubetkin[3], Sean P. Sylva[4], Zara Mirmalek[5,6],

4   Christopher R. German[4], and Darlene S. S. Lim[7]

5

6   [1]GEOPIG, School of Earth and Space Exploration, Arizona State University, Tempe, AZ 85287, USA

7   [*]vincentmilesi@hotmail.fr

8   [2]School of Molecular Sciences, Arizona State University, Tempe, AZ 85287, USA

9   [3]Ocean Exploration Trust, New London, CT 06320, United States

10   [4]Woods Hole Oceanographic Institution, Woods Hole, MA 02543, United States

11   [5]Harvard University, Cambridge, MA, United States

12   [6]Bay Area Environmental Research Institute, NASA Ames Research Park, Moffett Field, CA 94035,

13   Unites States

14   [7]Space Science and Astrobiology, NASA Ames Research Center, Moffett Field, CA 94035, United States

15

16

17

18

19   Key words: Ocean exploration, Ocean Worlds Analog, Forward geochemical modeling, Telepresence,

20   NASA PSTAR, E/V Nautilus, Information entropy

21

22   ABSTRACT

23   Maximizing scientific return is critical to the success of space exploration. During the SUBSEA project,

24   which explored the Sea Cliff vent site aboard the E/V *Nautilus* as an analog for hydrothermal systems on

25   Ocean Worlds, we used forward geochemical modeling to guide decision-making during the process of

26   exploration. Before the expedition, we performed 1670 reaction-path calculations to simulate water-rock

27   interactions during hydrothermal circulation covering wide ranges of reaction conditions, to predict the

28   diversity of possible chemical compositions and energy available for chemosynthetic microorganisms at

29   the Sea Cliff vents. Calculation of the information entropy of predicted concentrations of major solutes

30   and pH allowed us to identify dissolved silica as the chemical species capable of yielding the most

31   information about reaction conditions, and so the measurement of this parameter was implemented aboard

32   ship for our field-program. Using telepresence, results of onboard chemical analyses of fluid samples

33   collected during seafloor Dive *n* were sent to our shore-based scientific team, who processed the data and

34   used the outcomes to inform the design of Dive *n+2*. Combining data processing with forward modeling

35   revealed, within just two dives, that all the observed fluids venting from 10 to 300°C most likely resulted

36   from simple conservative mixing between seawater and a common hydrothermal fluid end-member: the

37   result of reaction of seawater with basalt at ≥350°C. Identification of these reaction conditions early

38   within the cruise allowed additional calculations to be performed to quantify the energy available from

39   redox disequilibria as a function of vent-fluid temperatures as they exited the seafloor. These calculations

40   can help inform and optimize real-time microbiological sampling and culture experiments onboard ship

41   during field expedition. The success of our approach coupling forward modeling and onboard ship

42   analyses allowed improved efficiency in completing of process studies at the Sea Cliff vent site, providing

43   time for further exploration and sampling of an additional, newly discovered vent site: Apollo. This study

44   demonstrates a novel application of forward and real-time modeling for scientific exploration which

45   allows the time required for result-informed decision making to be reduced from years to hours – an

46   essential breakthrough for future space exploration missions.

1. Introduction

Maximizing scientific return is critical when planning for space missions. The paradigm of scientific exploration often involves an experimental cycle in which data collection and analysis leads to new scientific insights, which fuel the design of new field investigations weeks to years to decades later. One way of maximizing scientific return is to achieve more knowledgeable decision-making at the time of exploration. This can be achieved by creating before exploration a framework of what to expect using modeling tools and then to compare expectations with observations in real-time, thereby reducing the time for result-informed decision making. Taking this approach is particularly promising for exploration of remote areas such as Earth's seafloor or extraterrestrial bodies, where the 'time on target' and the ability to return to areas of interest are commonly limited by environmental and operational constraints. In this context, telepresence, which consists of using telecommunications technology to simulate physical presence at a site other than one's true location (Minsky, 1980; Bell et al., 2015; Marlow et al., 2017), offers the possibility for shore-based modelers to engage in exploration, without increasing logistical and financial pressure unreasonably.

Among remote areas of astrobiological interests, seafloor hydrothermal systems have long-been recognized as possible environments for the emergence of life (Jannasch and Mottl, 1985; Shock, 1996). As part of the SUBSEA project (Lim et al., 2019, 2020), we visited in June 2019 the Sea Cliff hydrothermal vent field on the Gorda Ridge (Von Damm et al., 2006; Clague et al., 2020). Using two Remotely Operated Vehicle (ROVs), *Hercules* and *Argus*, that were operated by pilots on-board the E/V *Nautilus*, our team exploited telepresence to allow a shore-based scientific team, including geochemical modelers, to direct our seafloor investigations. Geochemical modeling enables the mapping of rock alteration, fluid compositions, redox gradients and related microbial communities. In this study, we used geochemical modeling to guide the exploration of the Sea Cliff vent site by using forward and real-time predictions to inform decision making about the design of our dive plans. Our methodological approach had three components:

72   - Before exploration began, thousands of reaction paths for water-rock interactions were

73   calculated, providing a library of possible fluid compositions occurring at Sea Cliff. The

74   chemical energy available in the vent fluids from redox disequilibria predicted to arise that

75   could fuel 16 candidate microbial metabolisms were also calculated. The modeling results

76   were analyzed using information entropy and this was used to identify which parameters

77   would be the most valuable to measure onboard ship to constrain the reaction conditions and,

78   hence, inform further exploration-oriented decision making.

79   - As our exploration progressed, those onboard ship analyses were relayed to shore where they

80   could be compared with the geochemical predictions to further refine operational priorities in

81   the field. Specifically, the goal was to appreciate, in real-time, how to achieve better informed

82   sampling to address two key questions: (i) whether the high-temperature focused Sea Cliff

83   vents were all fed by a single source, or multiple sources, at depth and (ii) whether any low-

84   temperature diffuse fluids present resulted from sub-surface low-temperature water-rock

85   interactions or from mixing between high-temperature hydrothermal fluids and seawater.

86   - Once the reaction conditions at the source for each type of vent fluids were constrained,

87   geochemical modelling was used to quantify the chemical energy available in fluids venting

88   across a range of temperatures at Sea Cliff to prioritize which specific sites would be most

89   valuable for astrobiology-related microbial investigations.

90   In this paper, we describe each step of the implementation of this methodological approach and show how

91   forward geochemical modeling coupled to deliberately chosen in-the-field measurements improves result-

92   informed decision making during scientific exploration.

93   **2. Geologic setting**

94   The Gorda Ridge, ca. 200 kms off the coast of Oregon and California, is an intermediate spreading-rate

95   mid-ocean ridge comprised of five offset segments (Figure 1). The spreading rate is 5.5 cm·yr^{-1} at the

96   northernmost segment where the Sea Cliff site is located (Wilson, 1993) and decreases to the south

97   (Chadwick et al., 1998). The northernmost segment displays steep axial walls that result from the

98   relatively high fraction of plate extension accommodated by normal faulting rather than magmatic

99   accretion (Shaw and Lin, 1993; Buck et al., 2005; Howell et al., 2016). The Sea Cliff vent field is located

100 2.6 km to the east of the axial rift-valley on the inward-facing wall at a depth of 2700-2750m ($\geq$ 300m

101 shallower than the rift valley floor) and on ocean crust that is ca.100,000 years old (Clague et al, 2020).

102 The site is extensive in terms of accumulated mineral deposits (>100m in diameter) and is surrounded by

103 pillow basalts (Zierenberg et al., 1995; Clague et al., 2020). Most of the hydrothermal vents that are

104 currently active occur in a linear zone, striking perpendicular to the ridge axis, climbing up the east wall

105 toward a small ridge. The clarity of the 300°C fluids is unusual compared to more typical (>350°C) mid-

106 ocean ridge vents where polymetallic sulfide minerals give rise to buoyant plumes of "black smoke",

107 making the origin of the fluids at Sea Cliff of particular interest (Von Damm et al., 2006). As described

108 previously (Von Damm et al., 2006), fluids sampled during our expedition were exiting from

109 hydrothermal chimneys that were typically 1-meter-high at most, made predominantly of anhydrite, and

110 extremely friable.
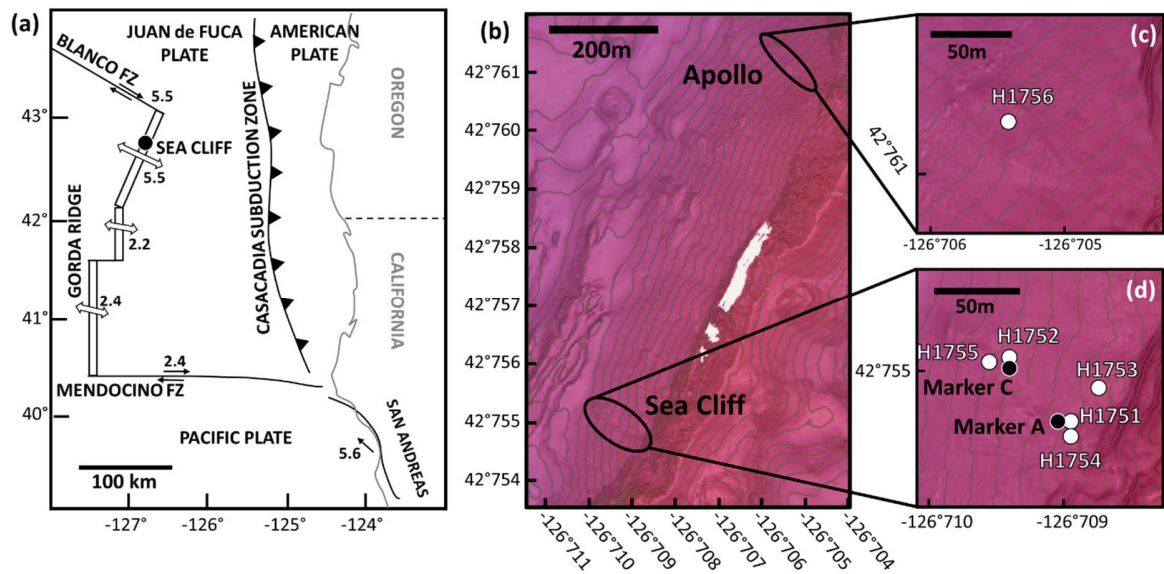
Figure 1. (a) Regional map of the Gorda Ridge showing the location of the Sea Cliff vent site and seafloor spreading rates (cm·yr^{-1}) (modified from Von Damm et al. (2006)). (b, c and d) Detailed location of the Sea Cliff and Apollo vent fields showing topography (10m contour line), the location of samples (open circles) and markers (closed circles). In map (a), spreading rates are in cm·yr^{-1}. In map (c) and (d), precision of the position of the sampling location is ±10 m.

3. Material and methods

3.1. Geochemical modeling

Geochemical modeling was performed with the EQ3/6 software (Wolery, 2010) and included thermodynamic data for minerals (Helgeson et al., 1978) and dissolved inorganic aqueous species (Shock and Helgeson, 1988; Shock et al., 1989, 1992, 1997; Sverjensky et al., 1997). In order to investigate a large range of possible reaction conditions at the origin of vent fluids at Sea Cliff, we used the programming language Python to automate the multiple runs and data processing of reaction path calculation following the approach of Ely (2020). Two reaction steps were considered in the reaction paths as illustrated in Figure 2. In Step 1, the consequences of sea water reacting with basalt from North Gorda Ridge (Table S 1) (Davis and Clague, 1987) were calculated in an open system along an increase

6

127 of temperature from 2°C to a temperature maximum T_{max} varying between 50 and 400°C, at intervals of

128 50°C. Calculations were done at a constant pressure of 500 bars. The rock/water ratio R/W, $i.e.$, the

129 amount of basalt in kg reacting with 1 kg of water, is defined by:

130
$$R/W_{Step1l} = \frac{xl}{350l} \qquad (1)$$

131   As listed in Table S 2, the amount of reacting basalt relative to water increases as the temperature

132 increases. A rock/water ratio of 1 is achieved at 350°C consistent with the literature (Von Damm et al.,

133 1985). To account for the influence of magmatic gases, a mixture of CO_2, SO_2 and H_2O gas is injected

134 during Step 1. The injected amount of gas, m in mol·kg^{-1} of basalt, is equal to:

135
$$m_{Step1l} = R/W_{Step1l} * lCl \qquad (2)$$

136 with C the gas content of average mid-ocean ridge basalt in mol·kg^{-1}, equal to 0.02, 0.03 and 0.05 mol·kg^{-1}

137 ^{1} for CO_2, SO_2 and H_2O, respectively (Table S 2) (Sakai et al., 1984; Gerlach, 1989; Holloway, 1998;

138 Wallace et al., 2015).
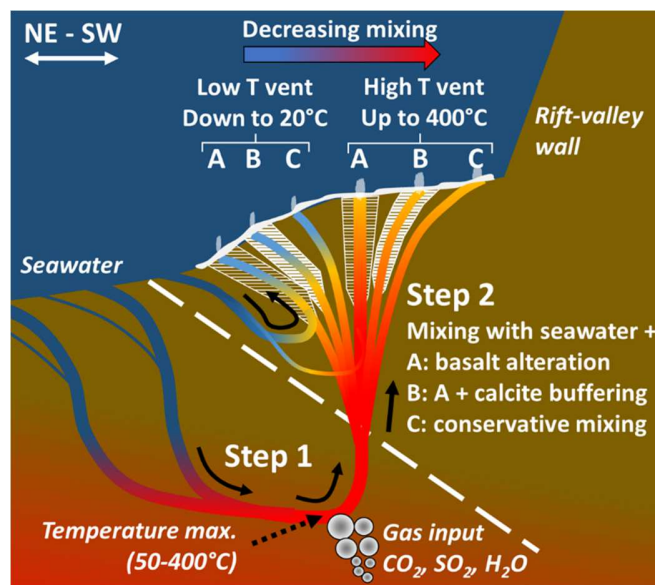
139

140 *Figure 2. Conceptual model of hydrothermal circulation at Sea Cliff. In Step 1, seawater reacts*

141 *progressively with basalt and volcanic gas (CO_2, SO_2 and H_2O) in an open system along an increase of*

142 *temperature from 2°C to a temperature maximum ranging from 50 to 400°C. In Step 2, the hydrothermal*

143 *fluid produced during Step 1 mixes with seawater in an open system from the temperature maximum to*

144 *20°C. The amounts of basalt and gas reacting during Step 2 are small fractions, F (0 to 10%), of those in*

145 *Step 1.Three regimes of chemical reactivity are considered during Step 2: equilibrium mixing (Model A),*

146 *equilibrium mixing while the fluid composition is buffered by calcite (Model B), conservative mixing in*

147 *which the speciation reactions proceed but the redox reactions, basalt dissolution and mineral*

148 *precipitation are suppressed (Model C).*

149   During Step 2, mixing occurs between the hydrothermal fluid end-member and sea water in an

150 open system from the temperature maximum to 20°C (Figure 2). Quartz precipitation is suppressed from

151 the calculation across all temperatures as kinetic limitations are expected to prevent its formation at low

152 temperature (Rimstidt and Barnes, 1980; Von Damm et al., 1991; Arvidson, 1999; Tivey, 2007). The

153 rock/water ratio and gas inputs during Step 2 are equal to:

154 $$R/W_{Step2} = F * \frac{x}{350} \tag{3}$$

155 and

156 $$m_{Step2} = R/W_{Step2} * C \tag{4}$$

157 with *F* equal to 0, 0.01, 0.02, 0.03, 0.05 or 0.1 as outlined in Table S 3. Thus, the amount of basalt and

158 gas reacting during Step 2 is a small fraction of those reacting during Step 1, which is meant to account

159 for rapid fluid flow and temperature decreases during upwelling and mixing. This study focuses on the

160 geochemical evolution of the fluids during Step 2 as those fluids are the ones eventually sampled at

161 seafloor.

162   Additional reaction conditions were investigated for Step 1, by adding multiplication coefficients

163 X_1 and X_2 to Equations 1 and 2, respectively, which become:

164 $$R/W_{Step1} = \frac{x}{350} * X_1 \tag{5}$$

165 and

166
$$m_{Step1l} \quad R/W_{Step1l} *lCl*lX_{2l} \tag{6}$$

167 where X_1 and X_2 can take independently the values of 0.5, 1, 2 and 4. This leads to a 4x4 matrix of sets of

168 reaction conditions for Step 1. Each of the 16 sets of reaction conditions contains 48 calculations (8

169 temperature maxima defining the rock/water ratio and the gas input of Step 1, and 6 F values for Step 2)

170 for a total of 768 reaction paths as summarized in Figure S 1.

171   The set of reaction paths described above were calculated for 3 regimes of chemical reactivity

172 during Step 2 summarized in Table S 4. In Model A and B, chemical equilibrium is considered. The

173 possibility that calcite influences the chemistry of the fluid during its upwelling toward surface, as

174 proposed by Von Damm et al. (2006), is investigated in Model B in which calcite buffers the fluid

175 composition throughout Step 2. In Model C, conservative mixing is considered during Step 2. Only the

176 speciation reactions proceed but the redox reactions, basalt dissolution and mineral precipitation are

177 suppressed. R/W_{Step2} equals 0 as it would lead to unrealistic solute concentrations.

178   When field data did not fit well with modeled results, additional calculations were performed

179 during exploration to explore reaction conditions not considered in Model A, B and C. Model B2 is a

180 refinement of Model B in which the influences of suppressing silicate mineral precipitation during Step 2

181 and removing the calcite buffer at various stages of Step 2 were investigated. Basalt dissolution is also

182 suppressed as it would lead to unrealistic solutes concentrations. For the sake of efficiency, the

183 temperature maximum, and the values of X_1, X_2 and F were fixed to 400°C, 1, 1 and 0, respectively. Thus,

184 the real-time modeling performed during exploration represents only a small fraction of that performed

185 before the expedition.

186   The EQ6 calculations provide *in situ* pH values for the hydrothermal fluid whereas pH is

187 measured onboard ship at ambient temperature and pressure. The pH change induced by the change from

188 *in situ* to ambient temperature and pressure was calculated by re-speciating all fluid compositions

9

189 throughout Step 2 to 25°C with charge balance on pH using EQ3. Mineral precipitation and redox

190 reactions were suppressed to account for the kinetic limitations expected during the quench of the fluid

191 samples. This calculation is opposite to what is commonly done for hydrothermal fluid samples, *i.e.* the

192 calculation of *in situ* pH using the fluid composition and pH measured at ambient temperature and

193 pressure (Reed and Spycher, 1984). The newly calculated pH is designated pH(25°C).
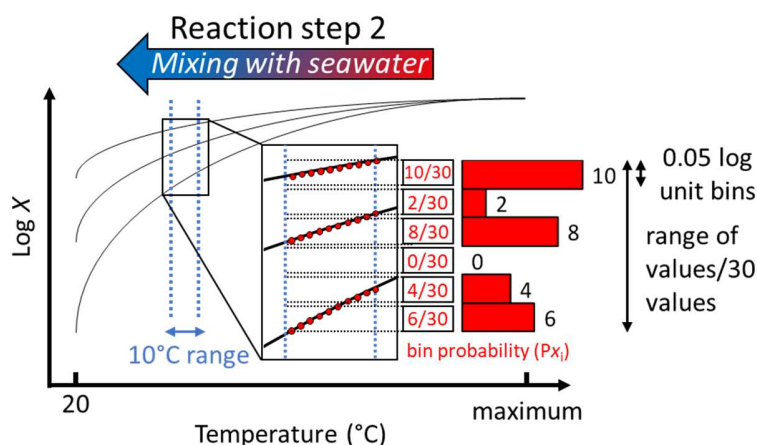
194 *3.2. Information entropy*

195 Information entropy was used to assess the chemical measurements that would best constrain the reaction

196 conditions. The information entropy is a quantification of the amount of information carried by the

197 occurrence of an event (Shannon, 1948). As the probability of an event to occur decreases, the

198 significance of its occurrence increases. Applied to thousands of modeled fluid compositions, the

199 information entropy of each chemical parameter reflects the diversity of values each parameter can take

200 as a response of the changing reaction conditions (Ely, 2020). For example, a given chemical parameter

201 whose value exhibits high diversity is greatly sensitive to changing reaction conditions. Its information

202 entropy is high, and its measurement would greatly inform about the reaction conditions. The information

203 entropy is written as:

$$204 \qquad H(X)l \quad -l\sum_{i=1}^{n} l P(x_i) log_2 P(x_i) l \qquad (7)$$

205 where *H* stands for the information entropy of a variable *X* with possible values $\{x_{1...} x_n\}$ and *P* represents

206 the probability of the variable *X* to take the value x_i. In the present study, *X* indicates a given chemical

207 parameter and $\{x_{1...} x_n\}$ the possible values it can take as a response of the changing reaction conditions.

208 The information entropy was calculated for the modeled values of pH, silica and major cations

209 (Na, Mg, K, Ca,) across Step 2 considering all reaction paths of Model A, B and C. Redox-sensitive

210 species were not considered because kinetic limitations may affect their behavior. The concentration of Cl

211 was also disregarded as it is not involved in the modeled water-rock interactions. The procedure for the

212 calculation of the information entropy of each chemical parameter is described in Figure 3. The decrease

213   in temperature during Step 2 from the temperature maximum (50-400°C) to 20°C is divided into 10°C

214   ranges and the information entropy is calculated for each. Inside a 10°C range, for each reaction path, the

215   value taken by the chemical parameter is considered every 1°C. A data set of all values across all reaction

216   paths for a given 10°C range is obtained. The range of values is then divided into bins. The probability of

217   each bin, or $P(x_i)$, is the ratio of the number of values contained in the bin over the total number of values

218   in the 10°C range. Calculation is done using a log scale to account for concentrations varying by orders of

219   magnitude. A bin width of 0.05 log unit was chosen. Decreasing the bin width results in a better

220   discretization of the probability of each value to occur but does not impact the relative value of the

221   information entropy between chemical parameters or between 10°C ranges. The information entropy is

222   normalized by the maximum value of information entropy obtained among all chemical parameters to

223   obtain the relative information entropy.

224

225   *Figure 3. Scheme describing the calculation of information entropy H for a chemical parameter X. The*

226   *decrease of temperature during Step 2 is divided into 10°C ranges (blue dotted vertical lines) and the*

227   *information entropy is calculated for each of them. Inside a 10°C range, for each reaction path (black*

228   *curve), the value taken by the parameter X is considered every 1°C (red dots). The range of values that*

229   *the parameter X takes across all reaction paths for a given 10°C range is divided into bins (black dotted*

11

230   *horizontal lines). The probability of each bin, or P(xᵢ), is the ratio of the number of values contained in*

231   *the bin over the total number of values in the 10°C range (red histogram).*

3.3. Bioenergetics calculation

233   The chemical energy available in the fluids during Step 2 for Model C, for which conservative mixing

234   between seawater and the hydrothermal fluid end-member produces chemical disequilibria, was

235   calculated for 16 inorganic redox reactions shown in Table 1. Given the composition of seawater and

236   seafloor hydrothermal fluids, these redox reactions are expected to yield considerable amounts of energy

237   supporting microbial metabolisms in vent fluids (McCollom and Shock, 1997; Shock and Canovas, 2010;

238   Amend et al., 2011; Nakamura and Takai, 2014; Reveillaud et al., 2016). The chemical affinity of a

239   reaction (A_r) is defined as

$$A_r = RT \ln(K_r/Q_r) \qquad (8)$$

241   where K_r stands for the equilibrium constant of reaction r in the standard conditions, R represents the gas

242   constant, T the temperature in Kelvin and Q_r the reaction quotient given as

$$Q_r = \prod_i a_i^{v_{i,r}} \qquad (9)$$

244   where a_i refers to the activity of the ith reactant or product, and $v_{i,r}$ stands for the stoichiometric reaction

245   coefficient of the ith component for the reaction r, with products being positive and reactants negative.

246   The extent to which reaction r can proceed and supply energy is determined by the concentration of the

247   limiting reactant *[lim]* divided by its stochiometric coefficient v_{lim}. Thus, the total amount of energy

248   available for a given reaction is defined by:

$$E_r = A_r \frac{[lim]}{v_{li}} \qquad (11)$$

250   *Table 1. Redox reactions considered for the bioenergetics calculations.*

| H₂ oxidation | $H_{2(aq)} + \frac{1}{2} O_{2(aq)} = H_2O$ |
| CO reduction | $3H_{2(aq)} + CO_{(aq)} = CH_{4(aq)} + H_2O$ |

CO oxidation	$CO_{(aq)} + \frac{1}{2} O_{2(aq)} = CO_{2(aq)}$
water-gas shift	$CO_{(aq)} + H_2O = CO_{2(aq)} + H_{2(aq)}$
autotrophic methanogenesis	$CO_{2(aq)} + 4H_{2(aq)} = CH_{4(aq)} + 2H_2O$
aerobic methanotrophy	$CH_{4(aq)} + 2O_{2(aq)} = CO_{2(aq)} + 2H_2O$
H_2S oxidation	$H_2S_{(aq)} + 2O_{2(aq)} = SO_4^{2-} + 2H^+$
SO_4^{2-} reduction	$SO_4^{2-} + 4H_{2(aq)} + 2H^+ = H_2S_{(aq)} + 4H_2O$
SO_4^{2-} methanotrophy	$CH_{4(aq)} + SO_4^{2-} + 2H^+ = CO_{2(aq)} + H_2S + 2H_2O$
H_2S denitrification	$NO_3^- + \frac{5}{8} H_2S = \frac{5}{8} SO_4^{2-} + \frac{1}{2} N_2 + \frac{1}{4} H^+ + \frac{1}{2} H_2O$
H_2 denitrification	$NO_3^- + 2.5H_2 + H^+ = \frac{1}{2} N_2 + 3H_2O$
NO_3^- reduction	$NO_3^- + 4H_{2(aq)} + 2H^+ = NH_4^+ + 3H_2O$
NO_3^- methanotrophy	$NO_3^- + H^+ + \frac{5}{8} CH_{4(aq)} = 0.5N_{2(aq)} + \frac{5}{8} CO_{2(aq)} + 1.75 H_2O$
NH_4^+ oxidation	$NH_4^+ + 2O_{2(aq)} = NO_3^- + 2H^+ + H_2O$
N_2 reduction	$N_{2(aq)} + 3H_{2(aq)} = 2NH_{3(aq)}$
Fe^{2+} oxidation	$4Fe^{2+} + O_{2(aq)} + 4H^+ = 4Fe^{3+} + 2H_2O$

3.4. Exploration operation

Two scientific teams participated in the exploration, one team located on the ship, the other one involved through telepresence form the University of Rhode Island. Seven dives of 8 hours each effectively spent on seafloor were carried out. To simulate some type of planetary operations, the shore-based team was only allowed to communicate once a day with the ship-based team through a report which included the dive plan of Dive *n+1*. This operational constraint led to the following work sequence. Chemical analyses of fluid samples were performed daily by the ship-based team. The analytical results of samples collected during Dive *n* were sent to the shore-based team to be processed with Model A, B and C during Dive *n+1* as illustrated in Figure S 2. The results were used by the shore-based team to inform the design of the dive and sampling plan for Dive *n+2*, sent to ship for implementation. During exploration, discrepancy between field data and model results motivated additional modeling efforts to investigate reaction conditions not considered in the pre-cruise modeling. The first dive was a reconnaissance of the Sea Cliff vent field and the subsequent dives were alternatively dedicated to the sampling of low-temperature (<120°C) and high-temperature (>120°C) fluids to serve the microbiological and geochemical purposes, respectively. In this work configuration, the sampling of a high-temperature dive (Dive *n*) influenced the dive plan of the following high-temperature dive (Dive *n+2*) and similarly for low-temperature dives.

268 Except for the reconnaissance dive, one sampling site was visited per dive for a total of 6 duplicate

269 samples and 4 result-informed dive plans.

270 *3.5. Sampling and onboard ship measurements*

271 At each site, a fluid sample and a duplicate were collected using an Isobaric Gas-Tight sampler (IGT)

272 (Seewald et al., 2002). The temperature was measured continuously during the 3 minutes that the IGT

273 sampling lasts, giving a way to directly monitor potential seawater contamination during sampling. The

274 pH value, and the CH_4 and H_2 concentrations are time-sensitive analyses required to be measured daily

275 onboard ship. Gas chromatography equipped with a Thermal Conductivity Detector (TCD) and a Flame

276 Ionization Detector (FID) was used to measure H_2 and CH_4, respectively, with detection limits of 3 μM

277 and 0.05 μM. The measurement of the Si concentration was specially implemented onboard ship based on

278 the results of the pre-cruise geochemical modeling. The Si concentration was measured as total dissolved

279 silica by spectrophotometry using the silico-molybdate method and portable Hach spectrometers. The

280 protocol was adapted assuming a salt content close to that of seawater and total sulfide concentration

281 close to millimolal (Von Damm et al., 2006). Tests showed that the salt content has no influence on the

282 measurement but that the presence of dissolved sulfide produces a yellow precipitate when adding the

283 silico-molybdate reagents. In such cases, the samples were acidified to an HCl concentration of 0.01M. In

284 the process, the dissolved sulfides turn into H_2S, which is then removed by purging the sample with N_2

285 gas for 5 minutes. A volume of 10 mL was needed for the spectrophotometric measurement. As most

286 samples required a 10-fold dilution for the silica concentration to be in the optimal range of concentration

287 of the method (1-100 ppm), a sample volume of 1 mL was enough for the analysis. Values of pH at

288 ambient temperature, and concentrations of Si, CH_4 and H_2 were measured on all 12 IGT samples. One

289 IGT sample leaked and six Si measurements did not work properly due to remaining sulfide interfering

290 with the silico-molybdate method and therefore these could not be included in the model comparisons.

291 **4. Results**

292 *4.1. Information entropy*

14

293   The Na, Ca, K, Mg, Si and pH(25°C) values of modeled fluids during Step 2 and their relative

294   information entropies are presented for Model A in Figure 4. The variability between reaction paths

295   involving a same temperature maximum stems from different rock/water ratios and gas inputs; however,

296   the latter parameters are less influential on the fluid composition than the temperature maximum. As

297   mineral precipitation depends on temperature, so do the concentrations of cations removed from or

298   supplied to the fluid during hydrothermal circulation.

299   The precipitation of albite fixes Na during the interaction of seawater with basalt at high

300   temperature (Seyfried et al., 1988). Consistently, as shown in Figure 5a, albite is at equilibrium with the

301   fluid at the beginning of Step 2 and equilibrates back again at the end of Step 2 for reaction paths for

302   which high basalt alteration (high R/W_{Step2} value) increases the Na, Si, and OH⁻ in solution. Despite the

303   formation of albite, the relative variation of Na concentration in response to the water-rock interaction is

304   low because of the high concentration of Na in seawater, resulting in a low information entropy (Figure

305   4a and g).

306   Ca and K have higher information entropies (Figure 4b, c, g and h). The effectiveness of Ca-

307   fixation by the precipitation of epidote and tremolite decreases with temperature (Seyfried et al., 1988,

308   1991; Berndt et al., 1989). Accordingly, at the beginning of Step 2, the modeled fluid compositions, at

309   equilibrium with epidote and tremolite (Figure 5b and c), have Ca concentration increasing with the

310   decrease of the temperature maximum, which results in relatively high information entropy of ca. 15%. K

311   is fixed naturally by the precipitation of muscovite at high-temperature and K-feldspar for advanced

312   oxidizing alteration at low-temperature (Alt, 1995). The modeled fluid compositions are at equilibrium

313   with muscovite at the beginning and during Step 2 and equilibrate with K-feldspar as the mixing

314   progresses, which results in an increase of the information entropy from <10 to 15% (Figure 5d, Figure

315   5e).

316   Mg uptake by mineral formation is most effective above 150°C (Seyfried and Bischoff, 1979), the

317   temperature at which clinochlore starts forming (Alt, 1995; Humphris and Klein, 2018). At the beginning

318   and during Step 2, the precipitation of talc and clinochlore (Figure 5f and g) results in the fixation of Mg

319   and high information entropy, >17% (Figure 4d and h). The diversity of Mg concentrations decreases

320   during Step 2 due to mixing with seawater. The Si concentration shows a great diversity of values below

321   250°C. The information entropy mostly above 16% increases at low-temperature due to K-feldspar

322   precipitation (Figure 4e and g). The pH(25°C) values are expected to be strongly dependent on the

323   reaction conditions as H^+ is involved in all precipitation reactions. Acidity is generated by Mg- and Ca-

324   fixation in talc, epidote and amphibole, the formation of which greatly depends on temperature.

325   Accordingly, pH(25°C) has the highest information entropy over the whole range of temperature with

326   values mostly above 16% (Figure 4f and h).

327   Which species shows the highest diversity of concentration is a function of the mixing extent and

328   therefore, the vent temperature. Over the whole range of temperature from 20 to 400ºC, pH(25°C) appears

329   as the most meaningful measurement; however, having to calculate the change of pH when bringing a

330   sample from *in situ* to ambient conditions creates a source of uncertainty, as assumptions must be made

331   on kinetic limitations hindering redox reactions and mineral precipitation during sample recovery. In light

332   of these uncertainties, the Si concentration appears to be the best parameter to constrain reaction

333   conditions of fluids venting below 250°C and was chosen to be measured on-board ship. Calculations of

334   the relative information entropies for Models B and C lead to similar conclusions (Figure S 3).

335
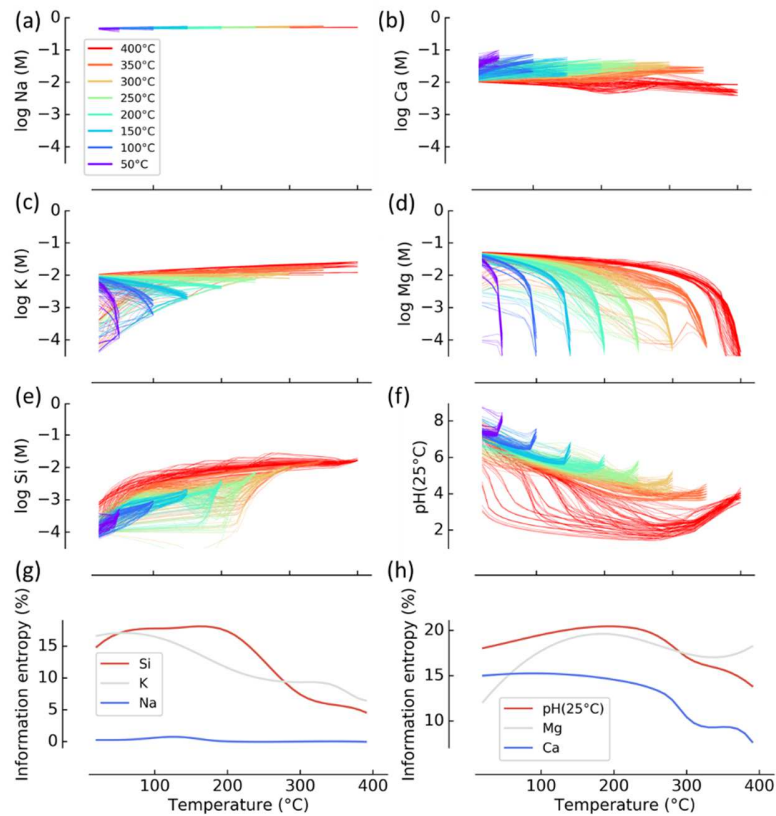
Figure 4. Modeled Na (a), Ca (b), K (c), Mg (d), Si (e) and pH(25°C) values (f) and their information

entropies (g, h) as functions of temperature during Step 2 for Model A. In plots (a) to (f), the color

gradation from purple to red represents the temperature maxima of the reaction paths from 50 to 400°C,

respectively. Curves of the same color correspond to reaction paths with the same temperature maximum

but different rock/water ratios and gas inputs.

17

341
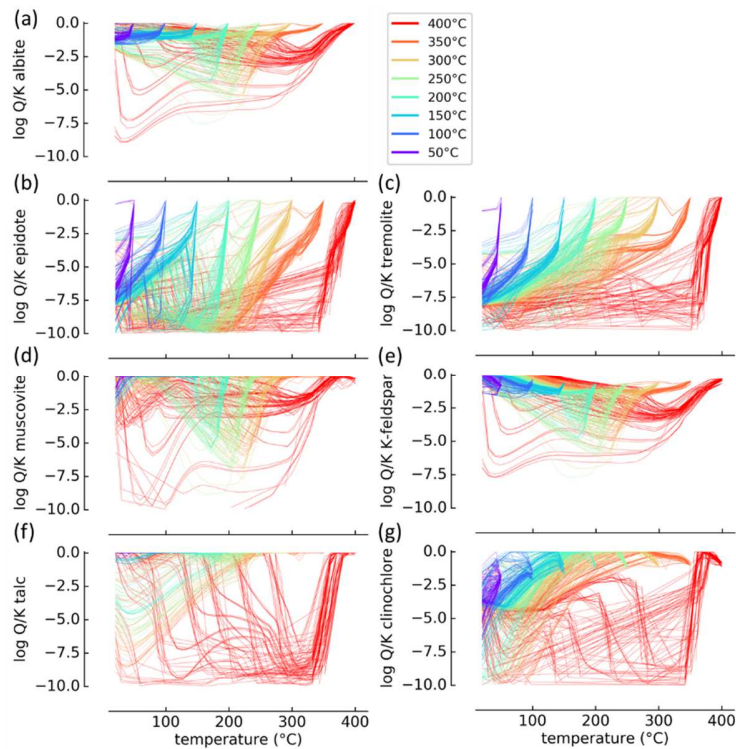
Figure 5. Saturation state of (a) albite, (b) epidote, (c) tremolite, (d) muscovite, (e) K-feldspar, (f) talc and (g) clinochlore during Step 2 for Model A. The color gradation from purple to red represents the temperature maxima of the reaction paths from 50 to 400°C, respectively. Curves of the same color correspond to reaction paths with the same temperature maximum but different rock/water ratios and gas inputs.

### 4.2. Modeled fluid composition

In Figure 6 to Figure 10, only the modeled composition of the fluids for pH(25°C), Si, H_2 and CH_4 are presented and discussed as those were the chemical parameters measured onboard ship. The results of the onboard ship analysis are discussed below in Section 4.4 to illustrate how comparing the onboard ship analyses with the forward geochemical modeling influenced our understanding of the Sea Cliff vent site, dive after dive. As shown in Figure 6, pH(25°C) values derived from Models A, B and C decrease with increasing temperature maximum, due to the increasing uptake of Mg and Ca in minerals as the temperature increases. Increases in rock/water ratio and gas input tend to increase and decrease the pH,

355 respectively, but overall generate less variability than the temperature maximum. In Model A and B, the

356 pH(25°C) values decrease at the beginning of Step 2, before increasing and converging toward the

357 seawater value as mixing progresses. This initial decrease of pH stems from the production of H^+ by

358 minerals precipitating as response to the supply of cations by seawater. In reaction paths involving a

359 temperature maximum of 400°C in Model A, pH(25°C) decreases dramatically at the beginning of mixing

360 and low pH values are maintained until high mixing extents. This results from the retrograde solubility of

361 anhydrite, which is expected to form during mixing of hydrothermal fluid end-members with seawater,

362 creating acidity (Bischoff and Seyfried, 1978; Janecky and Seyfried, 1984).

363   In Model B, buffering by calcite increases the pH(25°C) values compared to Model A and

364 decreases the variability introduced by the rock/water ratio and gas inputs. The pH(25°C) values of Model

365 C are close to those of Model B, with values increasing almost linearly during conservative mixing.
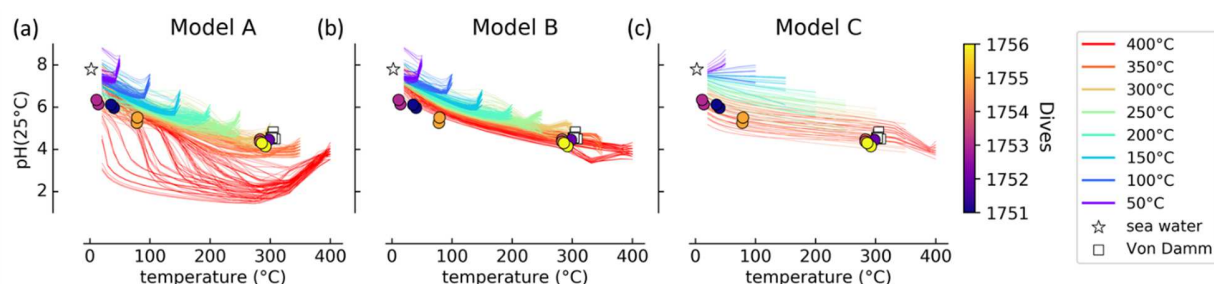
366

367 *Figure 6. Modeled pH(25°C) values as functions of temperature during Step 2 for Model A, B and C. The*

368 *color gradation from purple to red represents the temperature maximum of the reaction paths from 50 to*

369 *400°C, respectively. Curves of the same color correspond to reaction paths with the same temperature*

370 *maxima but different rock/water ratios and gas inputs. The open squares show the data of Von Damm et*

371 *al. (2006). The circles indicate samples in the present study, color-coded according to the dive during*

372 *which they were collected. The open star is the seawater value.*

373   As in the case of pH(25°C), the temperature maximum has a more influential effect on Si than

374 rock/water ratio or gas inputs. The Si concentrations of Models A, B and C increase with the temperature

19

375   maximum and decrease as mixing proceeds as shown in Figure 7. In Model A, the Si concentration is

376   controlled by mixing with seawater and the precipitation of muscovite and K-feldspar below 200ºC,

377   which increases with the alteration of basalt during Step 2 (Figure 7a). The Si concentration of Model B

378   drops massively at the beginning of mixing (Figure 7b). The high pH values induced by the calcite buffer

379   lead to the precipitation of clinochlore, which fixes Si (Figure S 4). The alteration of basalt induces a

380   subsequent increase of the Si concentration before it decreases again to converge toward the seawater

381   value. In Model C, the Si concentration is controlled by a conservative mixing between the hydrothermal

382   fluid end-member and seawater (Figure 7c).
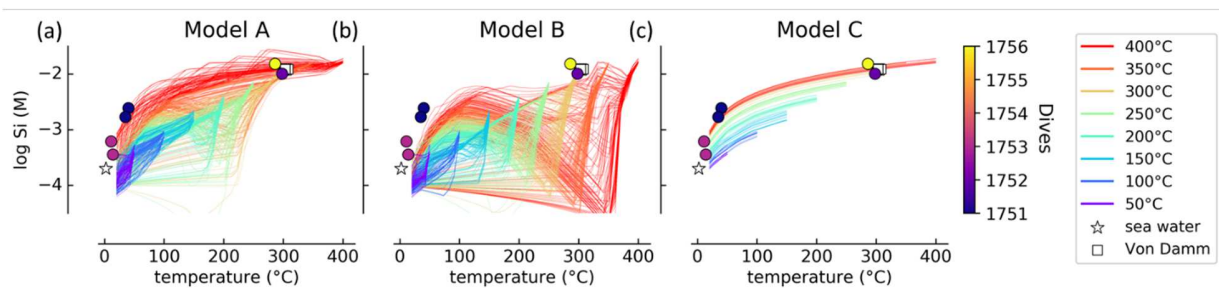
383

384 *Figure 7. Modeled Si concentrations as functions of temperature during Step 2 for Model A, B and C. The*

385 *color gradation from purple to red represents the temperature maximum of the reaction paths from 50 to*

386 *400°C, respectively. Curves of the same color correspond to reaction paths with the same temperature*

387 *maxima but different rock/water ratios and gas inputs. The open squares show the data of Von Damm et*

388 *al. (2006). The circles indicate the samples in this study, color-coded according to the dive during which*

389 *they were collected. The open star is the seawater value.*

390   Building on Models A, B and C that were performed before exploration, Model B2 was

391   performed during the cruise in light of the results of the onboard ship analyses to investigate reaction

392   conditions not considered in the pre-cruise models. For the sake of efficiency, the temperature maximum

393   and values of X_1, X_2 and F were fixed to 400°C, 1, 1 and 0, respectively, which were the most likely

394   reaction conditions inferred from field data at this time of the cruise. Thus, the reaction paths in Model B2

395   differ only by the mixing extent during which equilibrium with calcite is maintained. The suppression of

396   the calcite buffer at low mixing extent decreases the pH(25°C) values at the end of Step 2 as shown in

397   Figure 8a. Conservative mixing controls the Si concentration as basalt dissolution and the precipitation of

398   Si-bearing minerals are suppressed (Figure 8b).
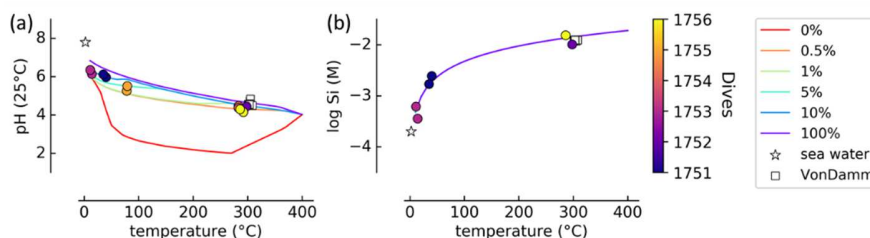

399

400   *Figure 8. Modeled values of pH(25°C) (a) and dissolved Si (b) as functions of temperature during Step 2*

401   *for Model B2. The colors spanning from red to purple represent mixing extent, in relative vol.%, during*

402   *which equilibrium with calcite is maintained. For instance, the blue curve corresponds to a reaction path*

403   *in which the fluid is maintained at equilibrium with calcite during the first 10 vol.% of mixing. The*

404   *temperature maximum and values of X_1, X_2 and F were fixed to 400°C, 1, 1 and 0, respectively. The open*

405   *squares show the data of Von Damm et al. (2006). The circles indicate the samples in this study, color-*

406   *coded according to the dive during which they were collected. The open star is the seawater value.*

407   The CH_4 and H_2 concentrations at the beginning of Step 2 increase with the temperature

408   maximum as shown in Figure 9 and Figure 10, respectively. At high temperature, H_2 is produced by the

409   oxidation of Fe^{2+}-bearing minerals in basalt (Bischoff and Seyfried, 1978; Alt, 1995; Humphris and Klein,

410   2018). In our models, the seawater- and basalt-derived CO_2 is reduced by H_2 into CH_4. The CH_4

411   concentration at the beginning of Step 2 represents a maximum as reduction of seawater-derived CO_2

412   during hydrothermal circulation is known to be sluggish (McDermott et al., 2015). The correlation

413   between CH_4 concentration and temperature maxima is no longer true for a temperature maximum of

414   >350°C as CO_2 becomes more stable than CH_4 and becomes the dominant carbon species. For reaction

415   paths with the same temperature maximum, higher rock/water ratios and lower gas inputs during Step 1

416   tend to produce higher H_2 concentrations in the hydrothermal fluid end-member. Increasing the gas input

417 tends to increase the CH_4 concentration at the expense of H_2 as CO_2 is the limiting reactant in the

418 formation of CH_4 from CO_2 reduction at high temperature. During mixing in Models A and B, the CH_4

419 and H_2 concentrations decrease dramatically due to the oxidizing species supplied by seawater that react

420 with H_2 and CH_4 to form H_2O and CO_2, respectively. For reaction paths with the same temperature

421 maximum, high R/W_{Step2} values maintain the CH_4 and H_2 concentrations close to nanomolal because the

422 supply of Fe^{2+} from basalt dissolution during fluid upwelling maintains relatively reduced conditions. The

423 H_2 and CH_4 concentrations of Model B2 (not shown) are similar than those of Models A and B as Model

424 B2 also involves equilibrium mixing during Step 2. In Model C, the CH_4 and H_2 concentrations are much

425 higher than in Model A, B and B2 as they are controlled by conservative mixing.
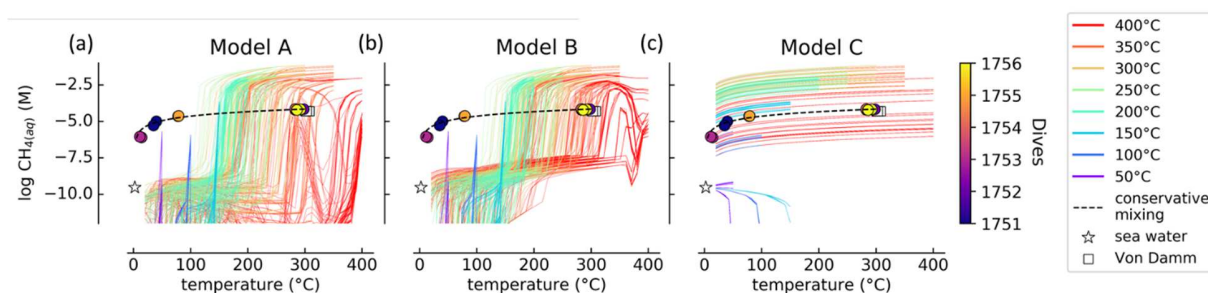
426

427 *Figure 9. Modeled CH_4 concentrations as functions of temperature during Step 2 for Model A, B and C.*

428 *The color gradation from purple to red represents the temperature maxima of the reaction paths from 50*

429 *to 400°C, respectively. Curves of the same color correspond to reaction paths with the same temperature*

430 *maximum but different rock/water ratios and gas inputs. The dashed curve represents the evolution of the*

431 *CH_4 concentration assuming conservative mixing between the H1754 sample and seawater. The open*

432 *squares show the data of (Von Damm et al., 2006). The circles indicate the samples in this study, color-*

433 *coded according to the dive during which they were collected. The open star is the seawater value.*

434
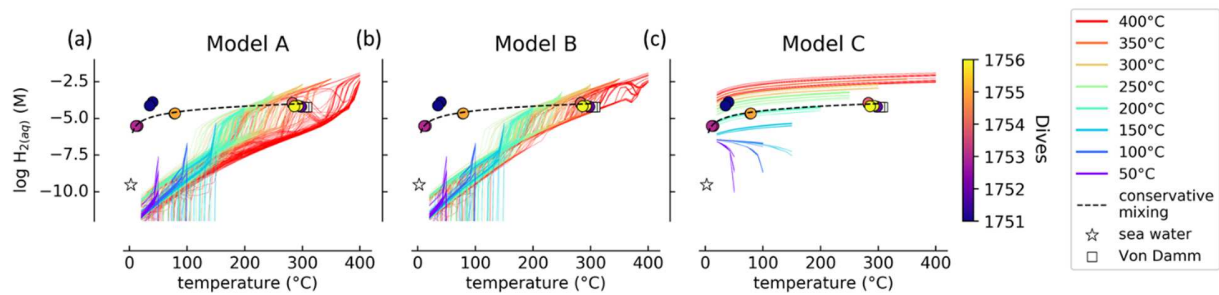
Figure 10. Modeled H_2 concentrations as functions of temperature during Step 2 for Model A, B and C. The color gradation from purple to red represents the temperature maxima of the reaction paths from 50 to 400°C, respectively. Curves of the same color correspond to reaction paths with a same temperature maximum but different rock/water ratios and gas inputs. The dashed curve represents the evolution of the H_2 concentration assuming a conservative mixing between the H1754 sample and seawater. The open squares show the data of Von Damm et al. (2006). The circles indicate the samples in this study, color-coded according to the dive during which they were collected. The open star is the seawater value.

4.3. Chemical energy

Chemosynthetic microbial communities in vent fluids thrive on the chemical energy that becomes available when hydrothermal fluids mix with seawater. Bioenergetics modeling, which predicts the amount of chemical energy available in fluids out of equilibrium for specific redox reactions, can be used to estimate the likelihood of microbial metabolisms to occur in vent fluids. Chemical energy forms when kinetic limitations prevent redox reactions to take place during mixing between a reduced hydrothermal fluid end-member and oxidized seawater, as simulated in Model C. The hydrothermal fluid end-member is enriched in H_2, CH_4, CO and H_2S produced by the reduction of seawater-derived sulfate (Figure S 5b) while seawater is enriched in oxidizing species, among which O_2, sulfate and nitrate. The chemical energies available from disequilibria in fluids involving 16 inorganic redox reactions evaluated via Model C are presented in Figure 11 and Figure 12. It should be noted that our calculations represent maximum amounts of energy. If part of the redox reactions were to occur abiotically (McDermott et al., 2020), there

23

454   would be less energy available compared to our calculations. In general, the available energy increases as

455   the temperature maxima and rock/water ratios increase and it increases as gas inputs decrease because of

456   increasing amounts of reducing species in the hydrothermal fluid end-member. For reactions involving

457   methane, and especially for anaerobic methanotrophy using SO_4^{2-}, the correlation between temperature

458   maximum and chemical energy no longer holds once the temperature maximum reaches 400°C, as CO_2

459   becomes more stable than CH_4 in the hydrothermal fluid end-member.

460   During mixing of the hydrothermal fluid end-member with seawater, an energy maximum is

461   reached for each reaction at the transition from conditions where the seawater-supplied oxidized species is

462   the limiting reactant in the redox reaction to those where the reduced species carried by the hydrothermal

463   fluid end-member becomes the limiting reactant. This energy maximum is achieved at different extents of

464   mixing depending on the reaction conditions and the redox reactions considered, which allows us to

465   identify two groups of redox reactions. In Group 1 (Figure 11), energy maxima are reached at high

466   extents of mixing. Additionally, the mixing extent corresponding to the energy maximum typically

467   increases with the temperature maximum of the hydrothermal fluid end-member because of the increasing

468   content of reduced species. For some reaction paths with a temperature maximum >200ºC, the energy

469   increases continuously throughout mixing with seawater. In these cases, the mixing extent at which the

470   reduced species becomes the limiting reactant is not reached over the range of mixing investigated. As

471   shown in Figure 11, the amounts of energy available from the redox reactions are relatively

472   homogeneous, ranging from 10 to 25 J·kg^{-1} and frequently reached at 20°C.

473   In contrast to Group 1, the redox reactions in Group 2 reached their energy maxima at lower

474   extents of mixing as illustrated in Figure 12. As a consequence, over the 0-130°C temperature range

475   suitable for life (Kashefi, 2003; Takai et al., 2008), these energy supplies mostly decrease from energy

476   maxima at 130ºC. Another contrast from Group 1 is that the amounts of energy in Group 2 vary widely

477   depending on the reaction. As examples, the water-gas shift reaction provides less than 0.1 J·kg^{-1}, the

478   energy available at 130°C from CO reduction, Fe^{2+} oxidation, and CO oxidation range from 5 to 10 J·kg^{-1},

479   and the maximum energy at 130°C varies from 80 to 150 J·kg^{-1} for N$_2$ reduction, autotrophic

480   methanogenesis, and SO$_4^{2-}$ reduction. The energy maximum for anaerobic methanotrophy using SO$_4^{2-}$ is

481   one order of magnitude higher, up to 1000 J·kg^{-1} at 130°C. It should be noted that, because the reduction

482   of seawater-derived CO$_2$, which is sluggish in natural systems (McDermott et al., 2015), occurs at

483   equilibrium in our models, the modeled CH$_4$ concentrations represent maximum values and, as

484   consequences, the bioenergetics calculation tends to maximize and minimize the energy supply from

485   redox reactions involving CH$_4$ as reactant and product, respectively.
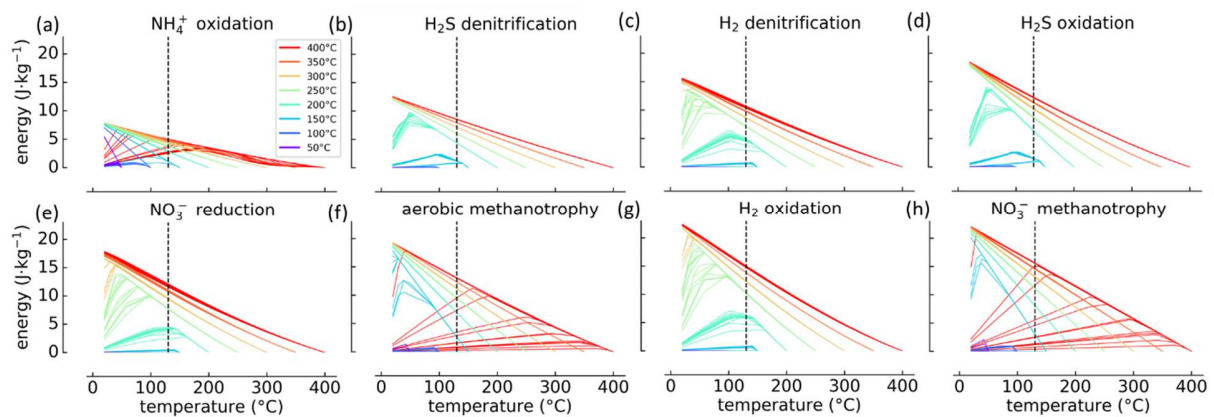
486

487   *Figure 11. Chemosynthetic energy of Group 1 reactions during Step 2 for Model C. The color gradation*

488   *from purple to red represents the temperature maxima of the reaction paths from 50 to 400°C,*

489   *respectively. The curves of the same color correspond to reaction paths with the same temperature*

490   *maximum but different rock/water ratios and gas inputs. The vertical dashed line indicates an*

491   *approximate temperature limit for life of 130°C.*

492
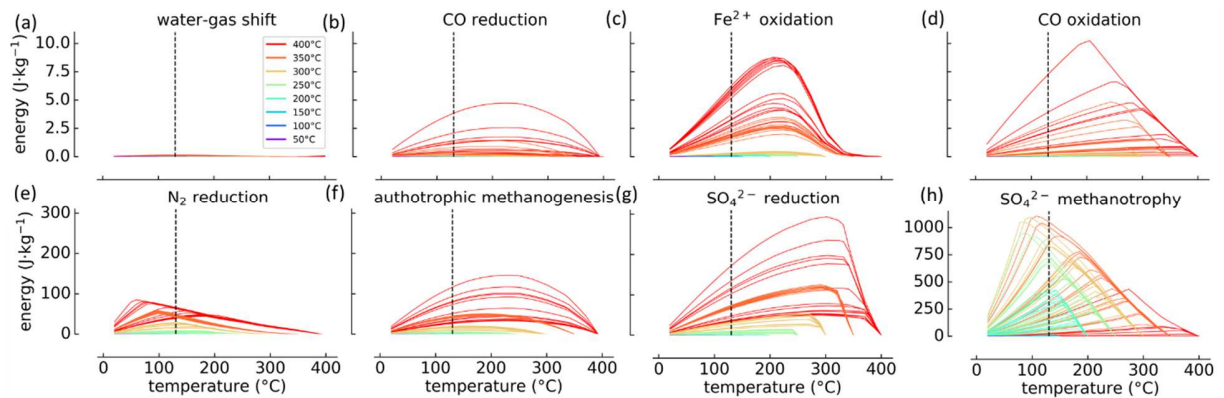
Figure 12. Chemosynthetic energy of Group 2 reactions during Step 2 for Model C. The color gradation from purple to red represents the temperature maxima of the reaction paths from 50 to 400°C, respectively. The curves of the same color correspond to reaction paths with the same temperature maximum but different rock/water ratios and gas inputs. The vertical dashed line indicates an approximate temperature limit for life of 130°C. The y-axis ranges from 0 to 11, 310, and 1150 J·kg⁻¹ for plots (a, b, d, d), (e, f, g), and (h), respectively.

5. Evolution of the seafloor exploration campaign

In this section, we show how the interrogation of onboard ship analyses using our forward geochemical modeling approach improved our understanding of the Sea Cliff vent site progressively, with each sequential dive, and guided the course of our exploration.

5.1. Pre-exploration studies

The only constraints on the fluid chemistry that existed prior to our SUBSEA expedition dated from a study of the same site in 2000 and 2002 (Von Damm et al., 2006). Those authors identified several fluid vents with maximum reported temperatures of ~300°C and an apparently constant end-member composition suggesting a single hydrothermal source at depth. Their pH(25°C) values and Si concentrations could be explained by our Model A, based on a maximum temperature of 300°C (Figure 6a and Figure 7a); however, the low Cl concentrations measured by Von Damm et al. (2006) suggested

510   that the fluids they sampled may have experienced liquid-vapor phase separation at depth, implying a

511   maximum temperature above 400°C at depth, beneath the seafloor. Considering reaction paths with

512   temperature maxima of 400°C, the pH(25°C) values of Model A are 2 to 3 pH units lower than those

513   measured by Von Damm et al. (2006), who had previously suggested that calcite veining within the old

514   ocean crust at the Sea Cliff site (perhaps inherited from a previous generation of hydrothermal activity

515   when the same crust was closer to the ridge-axis), could be buffering the chemistry of the modern-day

516   fluids during upwelling toward the seafloor. The reaction paths of Model B with a temperature maximum

517   of 400°C are, indeed, consistent with those measured pH values - but they cannot be reconciled so easily

518   with that team's reported Si concentrations (Figure 6b and Figure 7b). Considering the dissolved gas data

519   reported by Von Damm et al (2006), the measured CH_4 and H_2 concentrations are consistent with the

520   reaction paths of both Model A and Model B with a temperature maximum ≥350°C (Figure 9a and b,

521   Figure 10a and b). This indicates that CH_4 and H_2 could be oxidized under low extents of mixing (dilution

522   factor <1.33) while fluid temperatures remain higher than 300°C. Model C allows the previously reported

523   values for pH, Si and CH_4 concentrations to be reconciled with reaction paths involving a temperature

524   maximum of 400°C but it still cannot explain the observed H_2 concentrations (Figure 6c, Figure 7c,

525   Figure 9c, Figure 10c).

526   Thus, none of the models were adequate to completely explain the fluid compositions that had

527   been reported 20 and 18 years prior to the start of our field program. This knowledge gave our SUBSEA

528   program the impetus to investigate the occurrence and diversity of hydrothermal vents and associated

529   diffuse flow sites at Sea Cliff, their chemical composition, and the reaction conditions involved. Our

530   specific geochemical goals were to determine whether low-temperature water-rock interactions were

531   occurring or whether all compositions that we observed could be explained by simple two-component

532   mixing between high-temperature end-member vent fluids and seawater. At the outset of our expedition,

533   all results of Models A, B and C were considered equally plausible for the Sea Cliff site as illustrated in

534   Figure 13a.

535   *5.2. Dive H1751*

536   After an initial reconnaissance dive, Dive H1751 was dedicated to the sampling of a low-temperature

537   fluid (<120°C) and to a temperature probe survey to determine the diversity of high-temperature vents

538   available. The IGT sampling was performed on a fluid venting at 35-40°C on the eastern part of the ridge

539   formed by the hydrothermal vents at Marker A (Figure 1d). Sample temperatures are summarized in

540   Table 2. The temperature survey showed the presence of several sites where ~300°C fluid exits tens-of-

541   centimeters-high chimneys while diffusive fluid flow was observed at the bottom of the chimneys.

542   *5.3. Dive H1752*

543   Dive H1752 was dedicated to the sampling of a fluid with the highest available temperature to interrogate

544   how it compares with the high temperature fluids from Von Damm et al. (2006). The IGT sampling was

545   performed on a fluid venting out of a one-meter high chimney located in the western part of the vent field,

546   down the hydrothermal ridge at Marker C (Figure 1d). A temperature maximum of 298°C was recorded,

547   close to the temperature reported by Von Damm et al. (2006).

548   Meanwhile, the results of the H1751 sample analysis, shown in Table 2, were processed. No

549   matter which model is considered, the pH(25°C) value and the Si concentration of the 35-40°C fluid

550   sample are not consistent with reactions paths involving low-temperature maxima but rather suggest

551   mixing between a high-temperature fluid and seawater (Figure 6 and Figure 7). Considering Model A, the

552   pH(25°C) value and Si concentration are best explained by reaction paths with a temperature maximum of

553   400°C (Figure 6a and Figure 7a). If so, the H1751 sample and the fluids sampled by Von Damm et al.

554   (2006) could not be genetically related as the Cl depletion and the pH values in the latter fluid cannot be

555   reconciled within Model A. At least two hydrothermal fluid end-members supplying the same vent field

556   would have to be involved to explain the two kinds of fluid, which has been observed in shallow-sea

557   venting (e.g., Price et al., 2015).

558   None of the reaction conditions of Model B can explain the pH(25°C) and Si concentration of the

559   H1751 sample (Figure 6b and Figure 7b). Both Model A and B fail to explain the CH_4 and H_2

560   concentrations (Figure 9a and b, Figure 10a and b). In contrast, Model C, via reaction paths involving a

561   temperature maximum of 400°C, can explain the pH(25°C), Si and CH_4 values of the H1751 sample, as

562   well as those of Von Damm et al. (2006) (Figure 6c, Figure 7c, Figure 9c). Only the H_2 concentration is

563   inconsistent (Figure 10c). Considering a temperature maximum of 400°C, lower and higher H_2

564   concentrations would be expected in the H1751 sample and in the Von Damm et al. (2006) fluids,

565   respectively. Other processes would have to be invoked such as (1) H_2 oxidation during mixing down to

566   300°C as shown in Model A and B followed by conservative mixing from 300º to 20ºC as shown in

567   Model C or (2) H_2 generation through bacterial fermentation of organic substrates at low temperature.

568   At this stage, relying mostly on the Si concentration and pH values which offer more confidence

569   than redox-sensitive species, we concluded that both Model A and C with reaction paths involving a

570   temperature maximum of 400°C could explain the H1751 fluid composition whereas Model B and the

571   involvement of low temperature hydrothermal fluid end-members were ruled out as summarized in Figure

572   13b. In the case of Model C, the H1751 sample and the fluids from Von Damm et al. (2006) can be

573   genetically related to a single hydrothermal fluid end-member which is not possible with Model A.

574   *5.4. Dive H1753*

575   Dive H1753 was dedicated to the sampling of a low-temperature fluid and to an exploratory transect in

576   the northern area of Sea Cliff for which new mapping data are available (Clague et al., 2020). A 11-14°C

577   fluid venting out of a tube-worm rich area was sampled (Figure 1d). The exploratory transect led to the

578   discovery of a new hydrothermal vent field, named Apollo, ~800 m further north, populated by several

579   chimneys tens of centimeters high and looking like those at Sea Cliff (Shields et al., 2019).

580   In parallel, the analytical results of the H1752 sample were processed (Table 2). The chemical

581   composition of the 298°C fluid sample is close to those reported by Von Damm et al. (2006) and

582 consistent with either Model A or C considering a temperature maximum of 300°C and 400°C,

583 respectively (Figure 6 to Figure 10). At this stage, following Occam's razor principle that the explanation

584 that requires the fewest assumptions is the most likely, Model C appeared more likely than Model A

585 which requires the involvement of multiple hydrothermal fluid end-members to explain the low- and

586 high-temperature fluid compositions as summarized in Figure 13c. The constancy of the high-temperature

587 fluid composition over 17 years and the observation of several ~300°C fluid vents are consistent with a

588 single hydrothermal fluid end-member suppling the Sea Cliff vent field, providing further support to

589 Model C. Model B offers an explanation for the pH(25°C) values but not for the Si concentration which

590 led us to refine Model B into Model B2 in which the precipitation of Si-bearing minerals and basalt

591 alteration are suppressed during Step 2 (Figure 8, purple '100%' line). The hypothesis tested here was that

592 kinetic limitations prevent the dissolution and precipitation of silicate minerals during fluid upwelling but

593 not calcite from buffering the fluid composition. The Si concentrations of H1751 and H1752 samples and

594 of the Von Damm et al. (2006) fluids are consistent with Model B2 but the pH(25°C) value of the low

595 temperature sample remains overestimated and Model C is still the best fit.

596 A decision was made to focus the next high temperature dive on sampling a fluid in the 100-

597 200°C range, which should provide the most information on the reaction conditions as the information

598 entropies of Si and pH are maximized in this temperature range (Figure 4).

599 *5.5. Dive H1754*

600 Moderate-temperature fluids (100-200°C) were identified on a visual basis as a slight shimmering effect

601 coming out of the seafloor rather than out of tens-of-centimeters-high chimneys. Measured temperatures

602 varied from 20 to 280°C when moving the probe by only a couple of centimeters making it difficult to

603 sample a fluid with a stable temperature measurement in the 100-200°C range. Because of that, sampling

604 was eventually done on a 283°C fluid vent near Marker A as it combined focused flow with a trustworthy

605 temperature measurement different from the H1752 sample (*i.e.*, 298°C) (Figure 1d).The observations of

606   great gradients of temperature at the centimeter scale suggested that the low-temperature fluids (<120°C)

607   are the result of extremely shallow mixing, just centimeters below the seafloor.

608   The analytical results of the H1753 sample were processed (Table 2). Similar information is

609   retrieved from the analysis of the 11-14°C sample as from that of the H1751 sample (35-40°C) (Figure 6,

610   Figure 7). The fluid composition is consistent with Model A and C considering a temperature maximum

611   of 400°C, which implies, in the case of Model A, co-existence of multiple hydrothermal end-members to

612   reconcile low- and high-temperature vents. The CH_4 and H_2 concentrations, in good agreement with

613   Model C (Figure 9c, Figure 10c), suggest that no abiotic nor biologically driven oxidation occurs, which

614   is consistent with a rapid shallow mixing. Additional refinements of Model B2 were performed in which

615   the calcite buffer is removed at various stages of mixing (Figure 8, red to blue lines). At this stage of the

616   cruise, the observations suggested that the mixing between the ~300°C hydrothermal fluids and seawater

617   occurred just centimeters below the seafloor such that it is unlikely for calcite to buffer the fluid

618   composition during this mixing stage. Thus, the hypothesis tested with the refined Model B2 was that

619   calcite filling ancient hydrothermal veins is remobilized only when interacting at high temperature

620   (>300°C) with the hydrothermal fluid. Removing the calcite buffer at high mixing extent decreases the

621   pH(25°C) values at the end of Step 2, which fit the data better (Figure 8a), offering support for the

622   hypothesis.

623   The shallow mixing observed between seawater and the high temperature fluids is consistent with

624   Model C being able to reconcile both low- and high-temperature fluid chemistry. Model B2 is close to

625   Model C as it requires suppressing basalt alteration, the formation of silicate minerals, and calcite

626   buffering early during the fluid upwelling to offer consistency with the data. Thus, after the collection of

627   three fluid samples, the forward geochemical modeling coupled to the onboard ship analysis allowed us to

628   understand well the reaction conditions at Sea Cliff. In this context, we decided to focus the next high-

629   temperature dive on sampling fluids at the newly discovered vent site, Apollo (Shields et al., 2019).

630   *5.6. Dive H1755*

631   Dive H1755 was dedicated to the sampling of a low-temperature fluid at the bottom of the hydrothermal

632   chimney at Marker C. The temperature probe survey showed again centimeters-thin fluid flows with

633   temperature varying from 50 to 280°C. Sampling was performed on the most stable fluid flow available.

634   A temperature maximum of 79°C was recorded (Figure 1d).

635   Processing the results of the H1754 sample was the last chance to influence the course of

636   exploration (Table 2). The pH(25°C), CH_4 and H_2 values of the 283°C sample are close to the H1752

637   sample (298°C) and the data of Von Damm et al. (2006), confirming the presence of a single

638   hydrothermal fluid end-member stable for at least 17 years (Figure 6, Figure 9, Figure 10).

639   *5.7. Dive H1756*

640   The goal of the last dive was to sample the hydrothermal chimneys observed at the newly discovered

641   Apollo site (Figure 1c). The temperature probe survey showed several vigorous fluid flows coming out of

642   one-meter-high chimneys with temperature of ~290°C. A temperature maximum of 292°C was recorded

643   during sampling.

644   The analytical results of the H1755 sample were processed (Table 2). Consistent with previous

645   samples, the 79°C fluid sample is best explained by Models C or B2 (see Figure 6c, Figure 7c, Figure 8,

646   Figure 9c, Figure 10c). Model B overestimates the pH(25°C) value, and the CH_4 and H_2 concentrations by

647   orders of magnitude (Figure 6b, Figure 9b, Figure 10b) while Model A still requires multiple

648   hydrothermal fluid end-members to reconcile the low- and high-temperature fluid chemistry.

649   While the ship returned to port, the analytical results of the H1756 sample were processed. The

650   chemical composition of the Apollo fluid sample is close to that of the high-temperature fluids at Sea

651   Cliff, suggesting that a single hydrothermal fluid end-member supplies the two vent sites (Figure 6 to

652   Figure 10, Table 2).
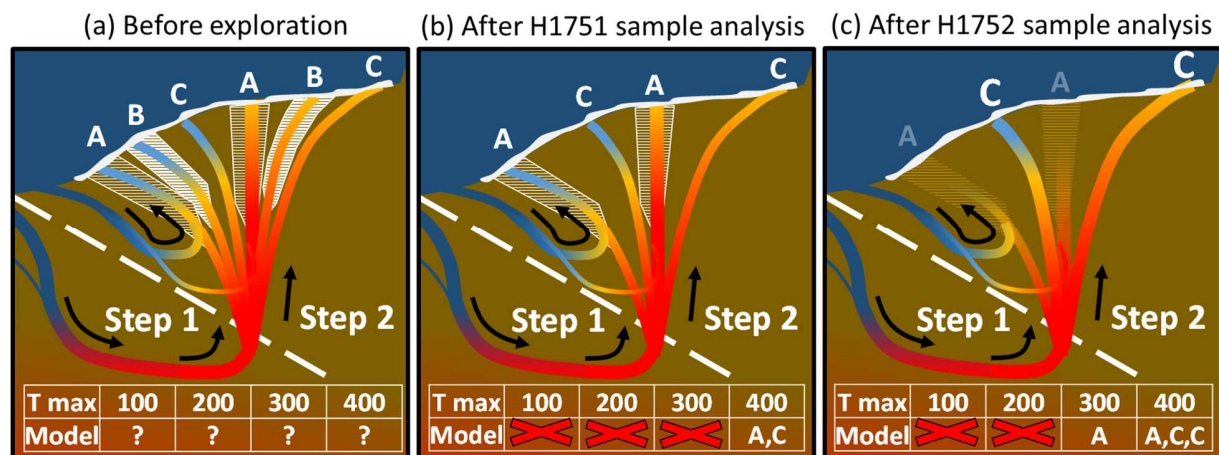
Figure 13. Evolution of our understanding of the reaction conditions at the origin of the Sea Cliff vent fluids as exploration progresses. Scheme (a), (b) and (c) summarize the hypotheses considered relevant before exploration and after the chemical analysis of the first (H1751) and the second (H1752) fluid sample, respectively. For clarity, the table at the bottom of each scheme represents a subset of the temperature maxima considered. A question mark indicates an open hypothesis. A red cross indicates that the sample analysis provides no evidence for the hypothesis. A, B or C indicates that the sample analysis offers support for the combination of a given temperature maximum with a given model (A, B or C). This marking is cumulative from scheme (b) to (c). Samples ≥H1753 are not represented as they just confirmed the information provided by sample H1751 and H1752.

Table 2. Onboard ship chemical analyses of fluid samples

Dive #	Sample ID[*]	Temp. max (°C)[a]	pH(25°C)	SiO_2(mM)[b]	CH_4 (μM)[b]	H_2 (μM)[b]
1751	H1751-IGT2	40	5.97	2.4	10	127
	H1751-IGT1	35	6.12	1.7	5	74
1752	H1752-IGT8	298	4.45	10.1	68	62
	H1752-IGT7			sample leaked		
1753	H1753-IGT2	14	6.14	0.4	1	b.d.
	H1753-IGT1	11	6.35	0.6	1	b.d.
1754	H1754-IGT7	283	4.47	inter.[c]	62	98
	H1754-IGT8	283	4.37	inter.	71	113
1755	H1755-IGT1	78	5.26	inter.	23	21
	H1755-IGT2	79	5.51	inter.	24	22

1756	H1756-IGT7	292	4.15	inter.	67	71
	H1756-IGT8	286	4.30	15.3	61	65

* The two samples collected during each dive are duplicates.

[a] temperature maximum recorded during IGT sampling

[b] Si as SiO_2 by spectrophotometry, CH_4 and H_2 by gas chromatography

[c] inter. stands for 'interference' and means that a yellow precipitate formed when adding the reagents of the silico-molybdate

method due to remaining H_2S, which interfere with the measurement.

b.d. stands for below detection limits which are of 3 µM and 0.05 µM for H_2 and CH_4, respectively


6. Bioenergetics calculations as guiding tools

Bioenergetics calculations makes it possible to rank redox reactions based on the energy they can supply to chemosynthetic microorganisms, which provides a prediction of the likelihood for microbial metabolisms to occur in vent fluids and upon mixing with seawater (McCollom and Shock, 1997; Shock and Canovas, 2010; Amend et al., 2011; Nakamura and Takai, 2014; Reveillaud et al., 2016). The better the reaction conditions at the source of the vent fluids are understood, the more the reliability of the bioenergetics calculations increases. After two dives, we were able to determine that the diffuse fluids were most likely the result of conservative mixing between seawater and a ≥350°C hydrothermal fluid end-member. From there, the maximum energy available from redox reactions in the low-temperature fluids, and especially in the fluid samples, could be calculated by considering all relevant reaction paths of Model C. Because that was not the initial intent for this project, those calculations, which make up a subset of the results presented in Figure 11 and Figure 12, were only completed post-exploration; however, they could have been performed during the cruise as soon as the reaction conditions were identified. Figure 14 presents the results for samples H1751, H1753 and H1755, which correspond to specific mixing extents and therefore specific vent temperatures. The energies supplied by reactions in Group 2, namely N_2 reduction, autotrophic methanogenesis, SO_4^{2-} reduction, and anaerobic methanotrophy using SO_4^{2-}, show a larger diversity of values over the range of possible reaction conditions when compared to those for reactions in Group 1. The energy from anaerobic methanotrophy

689 using SO_4^{2-} is one to two orders of magnitude greater than that of any of the other reactions, which mostly

690 fall within the range 10-20 J·kg^{-1}. With increasing temperature from sample H1753 to H1755 to H1751,

691 the energies from Group 2 reactions increase such that the reactions of N_2 reduction, autotrophic

692 methanogenesis, and SO_4^{2-} reduction progressively yield more energy than the Group 1 reactions whose

693 energies simultaneously decrease slightly. Therefore, for low temperature vent fluids such as sample

694 H1753, redox reactions from Group 1 and anaerobic methanotrophy using SO_4^{2-} are predicted to be the

695 most favorable metabolisms for microbes to exploit among the reactions considered. As the temperature

696 of vent fluids increases, the likelihood of these microbial metabolisms to supply energy decreases

697 whereas that of microbial metabolisms operating on the Group 2 reactions increases.

698   Our results are consistent with the study of Amend et al. (2011) in which the energy produced by

699 the mixing of seawater with representative hydrothermal fluids at vent fields hosted in various rock type

700 was calculated. As in our calculations, the energy yield from H_2-, CH_4-, and H_2S-oxidation increases as

701 the temperature of the fluid mixture decreases from 120 to 3℃. Overall, for vent-fluid temperature <40℃,

702 H_2, CH_4-, and H_2S-oxidation are the redox reactions yielding the most energy. Above 40℃, although

703 significant variations exist depending on the host rocks, the energy produced from methanogenesis and

704 sulfate reduction tends to increase relative to other reactions. In contrast to our study, anaerobic

705 methanotrophy using SO_4^{2-} in the study of Amend et al. (2011) yields low amounts of energy compared to

706 other reactions. This discrepancy may stem from the fact that, in our models, the production of CH_4 from

707 the reduction of seawater-derived CO_2, which is known to be sluggish in natural systems (McDermott et

708 al., 2015), leads to overestimates of the energy supply from redox reactions involving CH_4 as a reactant.

709   Future chemical and microbial analyses of the SUBSEA samples will allow more accurate

710 depictions of the bioenergetic landscape at Sea Cliff; however, our study demonstrates that, despite scarce

711 information about the Sea Cliff vent field before exploration, forward geochemical modeling coupled to

712 bioenergetics calculations allow predictions about the most favorable metabolisms for microbes in the Sea

713 Cliff vent fluids, which provides (1) a guiding tool for real-time microbial sampling and culture

714 experiments aboard ship, and (2) a testable hypothesis about microbial metabolisms in the Sea Cliff vent

715 fluids that will be returned to in an already planned study of microbial community structure and function

716 at the same site.
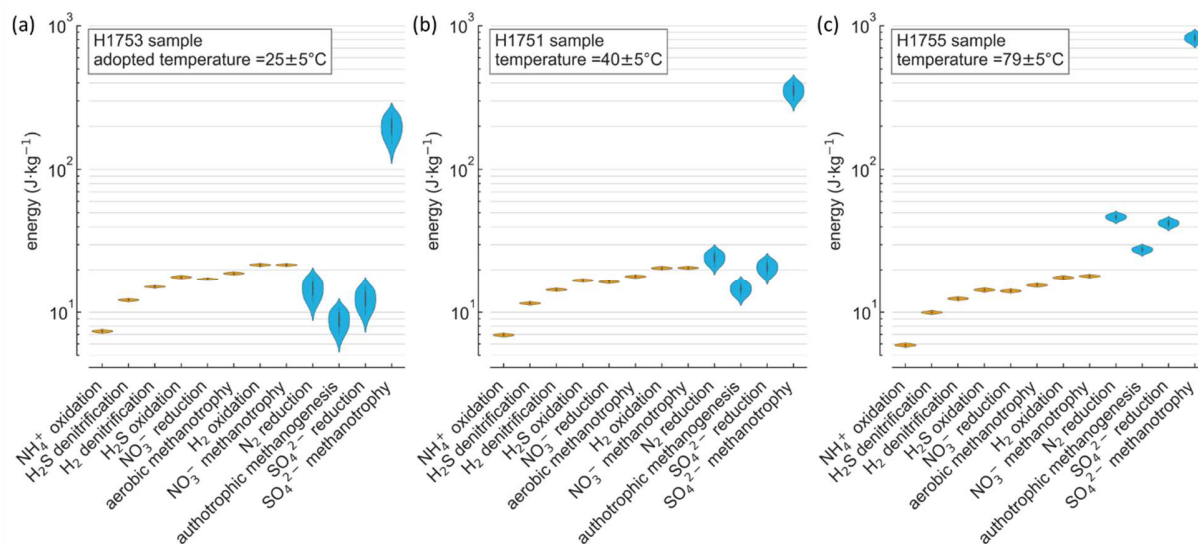
717

718 *Figure 14. Chemical energy (J·kg⁻¹) of samples H1753 (a), H1751 (b) and H1755 (c) from the redox*

719 *reactions of Group 1 (yellow violins) and Group 2 (blue violins), considering reactions paths of Model C*

720 *with temperature maxima ≥ 350°C. Only redox reactions supplying more than 1 J·kg⁻¹ are represented,*

721 *which excludes the water-gas shift reaction, CO reduction, Fe²⁺ oxidation, and CO oxidation. The shapes*

722 *of the violins show the probability density functions of chemical energies among the reaction paths*

723 *considered. A temperature of 25°C ±5°C is adopted for the H1753 sample as an approximation of the*

724 *measured temperature of 11-14°C because the models were set to stop once the fluid mixture reaches*

725 *20°C.*

726 *7. Exploration highlights*

727 By the end of the cruise, our forward modeling coupled with onboard ship analyses had enabled us to

728 demonstrate that (1) a single ≥350°C hydrothermal fluid end-member provides the source for submarine

729 venting at both the Sea Cliff and Apollo sites, (2) this source has most likely remained stable over a

730   timescale of ~20 years, (3) its conservative mixing with seawater in the shallow subsurface gives rise to

731   extensive diffuse flow emanating from the seafloor at temperatures as low as 10°C.

732   Applying information entropy to the outcomes of the forward geochemical modeling led us to

733   target exploration specifically for fluids in the 100-200°C range and to investigate co-located sites of

734   diffuse and high-temperature fluid flow just centimeters apart. The observations gained from that

735   fieldwork helped confirm geochemical evidence for shallow subsurface conservative mixing and

736   suggested that the hypothesized calcite buffering (Model B) was unlikely to occur. This led us to pursue

737   new data-driven modeling during the course of our exploration program. We showed that reaction paths

738   assuming partial equilibrium chemistry (no basalt dissolution nor Si-mineral precipitation) and dissolution

739   of calcite during part of the fluid upwelling, as proposed by Von Damm et al. (2006), could be consistent

740   with our pH and Si data, measured in the field, but that simple conservative mixing offered an alternative

741   explanation that better fits the measured vent-fluid H_2 and CH_4 concentrations.

742   The sample analyses that allowed us to determine subseafloor reaction conditions at Sea Cliff

743   were acquired early during our exploration program. The chemical composition of the first low-

744   temperature sample collected during Dive H1751, together with the end-member vent-fluid compositions

745   reported previously by Von Damm et al. (2006), already pointed toward a conservative mixing model.

746   Models assuming equilibrium chemistry appeared less likely, by comparison, because they required the

747   co-existence of multiple hydrothermal end-members to explain all of the fluid composition data. If the

748   Von Damm et al. (2006) data had not been available prior to our expedition, a minimum of two dives, one

749   each to sample a low- and a high-temperature vent site, would have been required to achieve a similar

750   level of preliminary understanding.

751   From there, and although it has only been done post-exploration in our study, bioenergetic

752   calculations could have been used during the cruise to inform the design of microbial sampling. At Sea

753   Cliff, the likelihood of sampling microbes with metabolisms that were capable of exploiting reactions in

754   Group 1 and Group 2 decreased and increased, respectively, with increasing vent temperature. Following

755 sample collection, bioenergetics calculations could also be used in the future to inform the choice of
756 chemical environments and settings for culture experiments aboard ship.

757   Once the analytical results are received by the geochemical modelers on shore, the computational
758 process of comparing onboard ship analyses with forward modeling outputs takes only a few seconds to
759 complete – a trivial proportion of the total time required to implement dive-planning protocols.   Of
760 course, when scientific exploration is being undertaken, it is inevitable that new data-driven hypotheses
761 will also be constructed. But these, again, can be tested in just a matter of a few hours via additional
762 reaction path calculations (e.g., Model B2). Thus, the time needed for result-informed decision-making
763 ranges from a few seconds to a couple of hours between dives. Because of operational constraints that
764 were adopted to simulate those of planetary exploration, we were not able to influence exploration on
765 such a short time scale during our 2019 SUBSEA expedition. Analyses for samples collected during Dive
766 *n* were only reported to shore after we had finalized plans for Dive *n+1* and, hence, could only be fed
767 forward to guide our investigations on Dive *n+2*. However, with the development of novel *in situ* sensors
768 that afford real-time data-visualization by the shore-based team, as is already possible for temperature and
769 a limited range of other parameters, result-informed decision-making will only become more powerful in
770 future using the pioneering methodological approach described here.

771 **8. Concluding remarks**

772 This study demonstrates the efficiency of forward and real-time geochemical modeling to maximize
773 scientific return during exploration of a hydrothermal vent site. In this first test-case, such an approach
774 allowed us to (1) identify the most meaningful measurements to be performed in the field, and (2)
775 accelerate our data processing to drastically reduce the time needed for result-informed decision making.

776   Applying information entropy to our model outputs allowed us to quantify the parameters that
777 would be the most informative to measure within the system under investigation. In this study, logistical
778 constraints meant that just one additional parameter could be implemented aboard ship and Si was

779 identified to be the most meaningful. However, our model outputs also showed that the choice of

780 parameter for which the information entropy is maximum actually varies as a function of venting

781 temperature. Consequently, we anticipate that in the future use of information entropy will allow a new

782 approach for *in situ* field measurements to emerge – one in which an array of the most meaningful

783 parameters to be measured can be chosen as a function of measured temperatures, in real-time during the

784 course of field exploration. Telepresence, by releasing part of the technical and logistical pressure

785 available *in situ* in the field, provides the opportunity and the intellectual space within which to

786 implement this new approach.

787 Current scientific field exploration often involves a multiyear experimental cycle, starting with

788 data and sample collection followed by analysis and modeling which leads to findings that influence the

789 design of subsequent experimental efforts. In this study, we used telepresence to implement the use of

790 forward and real-time geochemical modeling during seafloor exploration. This allowed us to reduce the

791 time needed for result-informed decision making to a timescale of hours and provided us with a core

792 understanding of the functioning of the Sea Cliff vent site after just two dives, liberating field-time for the

793 exploration of the newly discovered vent site, Apollo. Our ability to conduct model runs in real time, in

794 response to new data-driven assumptions, is promising for the exploration of extraterrestrial systems, for

795 which any initial (Earth-biased) hypotheses about the functioning of a completely unknown system may

796 quickly prove inappropriate.

797 Forward modeling also allows any bias induced by pre-existing knowledge to be minimized.

798 When modeling is relegated to the final stage of any project, only a limited number of models are built

799 and incrementally refined to interrogate the observations already selected for and completed. Such an

800 approach dates from an earlier time when calculation was time-consuming and expensive. Under those

801 conditions the design of theoretical models can be distorted by access to only a limited range of data,

802 making it difficult to resolve between multiple possible combinations of processes that could give rise to

803 a specific observation. Modern forward and real-time modeling, by contrast, allows us to explore a much

804 larger number of parameters, each varying over wide ranges of values thereby diminishing the influence

805 of bias inherited from pre-existing observations.

806   In the context of space exploration, the remoteness of extraterrestrial bodies, not least the ocean

807 worlds of the outer solar system, makes the maximization of scientific return an imperative. This study

808 shows that enabling real-time result-informed decision making can enable achieving that goal. In

809 addition, for all destinations where pre-existing data are scarce, we recommend the development of large

810 conceptual frameworks within which a wide range of reactions can be explored – an approach that will

811 simultaneously minimize any reliance upon Earth-based concepts to predict the conditions likely to be

812 encountered. In this context, forward and real-time geochemical modeling, coupled with information

813 entropy and implemented via telepresence appear highly promising for future missions to explore beyond

814 Earth, not least among other Ocean Worlds.

823

824

825 **REFERENCES**

826 Alt, J. C., 1995, Subseafloor processes in mid-ocean ridge hydrothermal systems: GEOPHYSICAL
827   MONOGRAPH-AMERICAN GEOPHYSICAL UNION, v. 91, p. 85–85.

828 Amend, J. P., T. M. McCollom, M. Hentscher, and W. Bach, 2011, Catabolic and anabolic energy for
829   chemolithoautotrophs in deep-sea hydrothermal systems hosted in different rock types:
830   Geochimica et Cosmochimica Acta, v. 75, no. 19, p. 5736–5748, doi:10.1016/j.gca.2011.07.041.

831 Arvidson, R. S., 1999, The dolomite problem; control of precipitation kinetics by temperature and
832   saturation state: American Journal of Science, v. 299, no. 4, p. 257–288,
833   doi:10.2475/ajs.299.4.257.

834 Bell, K. L. C., C. R. German, Z. Mirmalek, and A. Pallant, 2015, Transforming remotely conducted
835   research through ethnography, education, and rapidly evolving technologies (TREET):
836   Oceanography Supplement, v. 28, no. 1, p. 40–43.

837 Berndt, M. E., W. E. Seyfried Jr, and D. R. Janecky, 1989, Plagioclase and epidote buffering of cation
838   ratios in mid-ocean ridge hydrothermal fluids: Experimental results in and near the supercritical
839   region: Geochimica et Cosmochimica Acta, v. 53, no. 9, p. 2283–2300.

840 Bischoff, J. L., and W. E. Seyfried, 1978, Hydrothermal chemistry of seawater from 25 degrees to 350
841   degrees C: American Journal of Science, v. 278, no. 6, p. 838–860, doi:10.2475/ajs.278.6.838.

842 Buck, W. R., L. L. Lavier, and A. N. B. Poliakov, 2005, Modes of faulting at mid-ocean ridges: Nature, v.
843   434, no. 7034, p. 719–723, doi:10.1038/nature03358.

844 Chadwick, W. W., R. W. Embley, and T. M. Shank, 1998, The 1996 Gorda Ridge eruption: geologic
845   mapping, sidescan sonar, and SeaBeam comparison results: Deep Sea Research Part II: Topical
846   Studies in Oceanography, v. 45, no. 12, p. 2547–2569, doi:10.1016/S0967-0645(98)00083-6.

847 Clague, D. A., J. B. Paduan, D. W. Caress, J. McClain, and R. A. Zierenberg, 2020, Lava Flows Erupted
848   in 1996 on North Gorda Ridge Segment and the Geology of the Nearby Sea Cliff Hydrothermal
849   Vent Field From 1-M Resolution AUV Mapping: Frontiers in Marine Science, v. 7, p. 27,
850   doi:10.3389/fmars.2020.00027.

851 Davis, A. S., and D. A. Clague, 1987, Geochemistry, mineralogy, and petrogenesis of basalt from the
852   Gorda Ridge: Journal of Geophysical Research: Solid Earth, v. 92, no. B10, p. 10467–10483,
853   doi:10.1029/JB092iB10p10467.

854 Ely, T., 2020, Thermodynamic Cartography in Basalt-Hosted Hydrothermal Systems, Doctoral
855   dissertation: Tempe, Arizona State University.

856 Gale, A., C. A. Dalton, C. H. Langmuir, Y. Su, and J.-G. Schilling, 2013, The mean composition of ocean
857   ridge basalts: MEAN MORB: Geochemistry, Geophysics, Geosystems, v. 14, no. 3, p. 489–518,
858   doi:10.1029/2012GC004334.

859 Gerlach, T. M., 1989, Degassing of carbon dioxide from basaltic magma at spreading centers: II. mid-
860   oceanic ridge basalts: Journal of Volcanology and Geothermal Research, v. 39, no. 2–3, p. 221–
861   232, doi:10.1016/0377-0273(89)90061-9.

862 Helgeson, H. C., J. M. Delany, N. W. Nesbitt, and D. K. Bird, 1978, Summary and critique of the
863   thermodynamic properties of rock-forming minerals: American Journal of Science, v. 278, no. 1–
864   229.

865 Holloway, J. R., 1998, Graphite-melt equilibria during mantle melting: constraints on CO2 in MORB
866   magmas and the carbon content of the mantle: Chemical Geology, v. 147, no. 1–2, p. 89–97,
867   doi:10.1016/S0009-2541(97)00174-5.

868 Howell, S. M., G. Ito, M. D. Behn, F. Martinez, J.-A. Olive, and J. Escartín, 2016, Magmatic and tectonic
869   extension at the Chile Ridge: Evidence for mantle controls on ridge segmentation: CHILE
870   RIDGE EXTENSION AND SEGMENTATION: Geochemistry, Geophysics, Geosystems, v. 17,
871   no. 6, p. 2354–2373, doi:10.1002/2016GC006380.

872 Humphris, S. E., and F. Klein, 2018, Progress in Deciphering the Controls on the Geochemistry of Fluids
873   in Seafloor Hydrothermal Systems: Annual Review of Marine Science, v. 10, no. 1, p. 315–343,
874   doi:10.1146/annurev-marine-121916-063233.

875 Janecky, D. R., and W. E. Seyfried, 1984, Formation of massive sulfide deposits on oceanic ridge crests:
876   Incremental reaction models for mixing between hydrothermal solutions and seawater:
877   Geochimica et Cosmochimica Acta, v. 48, no. 12, p. 2723–2738, doi:10.1016/0016-
878   7037(84)90319-3.

879 Jannasch, H. W., and M. J. Mottl, 1985, Geomicrobiology of Deep-Sea Hydrothermal Vents: Science, v.
880   229, no. 4715, p. 717–725, doi:10.1126/science.229.4715.717.

881 Kashefi, K., 2003, Extending the Upper Temperature Limit for Life: Science, v. 301, no. 5635, p. 934–
882   934, doi:10.1126/science.1086823.

883 Lim, D. S. S. et al., 2019, SUBSEA 2018 Expedition to the Lōʻihi Seamount, Hawaiʻi (New Frontiers in
884   Ocean Exploration: The E/V Nautilus, NOAA Ship Okeanos Explorer, and R/V Falkor 2018
885   Field Season): Oceanography, v. 32, no. 1, p. 48–49, doi:10.5670/oceanog.2019.supplement.01.

886 Lim, D. S. S. et al., 2020, SUBSEA 2019 Expedition to the Gorda Ridge (New Frontiers in Ocean
887   Exploration: The E/V Nautilus, NOAA Ship Okeanos Explorer, and R/V Falkor 2019 Field
888   Season): Oceanography, v. 33, no. 1, p. 1–122, doi:10.5670/oceanog.2020.supplement.01.

889 Marlow, Jeffrey, C. Borrelli, S. P. Jungbluth, C. Hoffman, Jennifer Marlow, P. R. Girguis, and the AT-36
890   Team, 2017, Opinion: Telepresence is a potentially transformative tool for field science:
891   Proceedings of the National Academy of Sciences, v. 114, no. 19, p. 4841–4844,
892   doi:10.1073/pnas.1703514114.

893 McCollom, T. M., and E. L. Shock, 1997, Geochemical constraints on chemolithoautotrophic metabolism
894   by microorganisms in seafloor hydrothermal systems: Geochimica et Cosmochimica Acta, v. 61,
895   no. 20, p. 4375–4391, doi:10.1016/S0016-7037(97)00241-X.

896 McDermott, J. M., J. S. Seewald, C. R. German, and S. P. Sylva, 2015, Pathways for abiotic organic
897   synthesis at submarine hydrothermal fields: Proceedings of the National Academy of Sciences, v.
898   112, no. 25, p. 7668–7672, doi:10.1073/pnas.1506295112.

899 McDermott, J. M., S. P. Sylva, S. Ono, C. R. German, and J. S. Seewald, 2020, Abiotic redox reactions in
900   hydrothermal mixing zones: Decreased energy availability for the subsurface biosphere:
901   Proceedings of the National Academy of Sciences, v. 117, no. 34, p. 20453–20461.

902   Minsky, M., 1980, Telepresence.

903   Nakamura, K., and K. Takai, 2014, Theoretical constraints of physical and chemical properties of
904   hydrothermal fluids on variations in chemolithotrophic microbial communities in seafloor
905   hydrothermal systems: Progress in Earth and Planetary Science, v. 1, no. 1, p. 5,
906   doi:10.1186/2197-4284-1-5.

907   Price, R. E., D. E. LaRowe, F. Italiano, I. Savov, T. Pichler, and J. P. Amend, 2015, Subsurface
908   hydrothermal processes and the bioenergetics of chemolithoautotrophy at the shallow-sea vents
909   off Panarea Island (Italy): Chemical Geology, v. 407–408, p. 21–45,
910   doi:10.1016/j.chemgeo.2015.04.011.

911   Reed, M., and N. Spycher, 1984, Calculation of pH and mineral equilibria in hydrothermal waters with
912   application to geothermometry and studies of boiling and dilution: Geochimica et Cosmochimica
913   Acta, v. 48, no. 7, p. 1479–1492, doi:10.1016/0016-7037(84)90404-6.

914   Reveillaud, J., E. Reddington, J. McDermott, C. Algar, J. L. Meyer, S. Sylva, J. Seewald, C. R. German,
915   and J. A. Huber, 2016, Subseafloor microbial communities in hydrogen-rich vent fluids from
916   hydrothermal systems along the Mid-Cayman Rise: Subseafloor microbes at Mid-Cayman Rise:
917   Environmental Microbiology, v. 18, no. 6, p. 1970–1987, doi:10.1111/1462-2920.13173.

918   Rimstidt, J. D., and H. L. Barnes, 1980, The kinetics of silica-water reactions: Geochimica et
919   Cosmochimica Acta, v. 44, no. 11, p. 1683–1699, doi:10.1016/0016-7037(80)90220-3.

920   Sakai, H., D. J. D. Marais, A. Ueda, and J. G. Moore, 1984, Concentrations and isotope ratios of carbon,
921   nitrogen and sulfur in ocean-floor basalts: Geochimica et Cosmochimica Acta, v. 48, no. 12, p.
922   2433–2441, doi:10.1016/0016-7037(84)90295-3.

923   Seewald, J. S., K. W. Doherty, T. R. Hammar, and S. P. Liberatore, 2002, A new gas-tight isobaric
924   sampler for hydrothermal fluids: Deep Sea Research Part I: Oceanographic Research Papers, v.
925   49, no. 1, p. 189–196, doi:10.1016/S0967-0637(01)00046-2.

926   Seyfried, W. E., M. E. Berndt, and J. S. Seewald, 1988, Hydrothermal alteration processes at mid-ocean
927   ridges; constraints from diabase alteration experiments, hot spring fluids and composition of the
928   oceanic crust: The Canadian Mineralogist, v. 26, no. 3, p. 787–804.

929   Seyfried, W. E., and J. L. Bischoff, 1979, Low temperature basalt alteration by sea water: an experimental
930   study at 70°C and 150°C: Geochimica et Cosmochimica Acta, v. 43, no. 12, p. 1937–1947,
931   doi:10.1016/0016-7037(79)90006-1.

932   Seyfried, W. E., K. Ding, and M. E. Berndt, 1991, Phase equilibria constraints on the chemistry of hot
933   spring fluids at mid-ocean ridges: Geochimica et Cosmochimica Acta, v. 55, no. 12, p. 3559–
934   3580, doi:10.1016/0016-7037(91)90056-B.

935   Shannon, C. E., 1948, A Mathematical Theory of Communication: Bell System Technical Journal, v. 27,
936   no. 3, p. 379–423, doi:10.1002/j.1538-7305.1948.tb01338.x.

937   Shaw, P. R., and J. Lin, 1993, Causes and consequences of variations in faulting style at the Mid-Atlantic
938   Ridge: Journal of Geophysical Research: Solid Earth, v. 98, no. B12, p. 21839–21851,
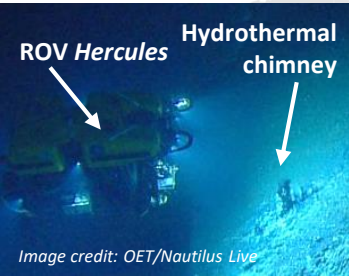939   doi:10.1029/93JB01565.

940   Shields, A., A. Garcia, S. K. Nawotniak, D. S. S. Lim, and N. A. Raineault, 2019, Discovering the Apollo
941   Deep Sea Hydrothermal Vent Field at Northern Gorda Ridge, Using Bathymetric Data.

942   Shock, E. L., 1996, Hydrothermal systems as environments for the emergence of life: Evolution of
943   hydrothermal ecosystems on Earth (and Mars, v. 202, p. 40–60.

944   Shock, E., and P. Canovas, 2010, The potential for abiotic organic synthesis and biosynthesis at seafloor
945   hydrothermal systems: Geofluids, doi:10.1111/j.1468-8123.2010.00277.x.

946   Shock, E. L., and H. C. Helgeson, 1988, Calculation of the thermodynamic and transport properties of
947   aqueous species at high pressures and temperatures: Correlation algorithms for ionic species and
948   equation of state predictions to 5 kb and 1000°C: Geochimica et Cosmochimica Acta, v. 52, no.
949   8, p. 2009–2036, doi:10.1016/0016-7037(88)90181-0.

950   Shock, E. L., H. C. Helgeson, and D. A. Sverjensky, 1989, Calculation of the thermodynamic and
951   transport properties of aqueous species at high pressures and temperatures: Standard partial molal
952   properties of inorganic neutral species: Geochimica et Cosmochimica Acta, v. 53, no. 9, p. 2157–
953   2183, doi:10.1016/0016-7037(89)90341-4.

954   Shock, E. L., E. H. Oelkers, J. W. Johnson, D. A. Sverjensky, and H. C. Helgeson, 1992, Calculation of
955   the thermodynamic properties of aqueous species at high pressures and temperatures. Effective
956   electrostatic radii, dissociation constants and standard partial molal properties to 1000 °C and 5
957   kbar: J. Chem. Soc., Faraday Trans., v. 88, no. 6, p. 803–826, doi:10.1039/FT9928800803.

958   Shock, E. L., D. C. Sassani, M. Willis, and D. A. Sverjensky, 1997, Inorganic species in geologic fluids:
959   Correlations among standard molal thermodynamic properties of aqueous ions and hydroxide
960   complexes: Geochimica et Cosmochimica Acta, v. 61, no. 5, p. 907–950, doi:10.1016/S0016-
961   7037(96)00339-0.

962   Sverjensky, D. A., E. L. Shock, and H. C. Helgeson, 1997, Prediction of the thermodynamic properties of
963   aqueous metal complexes to 1000°C and 5 kb: Geochimica et Cosmochimica Acta, v. 61, no. 7,
964   p. 1359–1412, doi:10.1016/S0016-7037(97)00009-4.

965   Takai, K., K. Nakamura, T. Toki, U. Tsunogai, M. Miyazaki, J. Miyazaki, H. Hirayama, S. Nakagawa, T.
966   Nunoura, and K. Horikoshi, 2008, Cell proliferation at 122 C and isotopically heavy CH4
967   production by a hyperthermophilic methanogen under high-pressure cultivation: Proceedings of
968   the National Academy of Sciences, v. 105, no. 31, p. 10949–10954,
969   doi:10.1073/pnas.0712334105.

970   Tivey, M. K., 2007, Generation of seafloor hydrothermal vent fluids and associated mineral deposits:
971   Oceanography, v. 20, no. 1, p. 50–65.

972   Von Damm, K. L., J. L. Bischoff, and R. J. Rosenbauer, 1991, Quartz solubility in hydrothermal
973   seawater; an experimental study and equation describing quartz solubility for up to 0.5 M NaCl
974   solutions: American Journal of Science, v. 291, no. 10, p. 977–1007, doi:10.2475/ajs.291.10.977.

975   Von Damm, K. L., J. M. Edmond, B. Grant, C. I. Measures, B. Walden, and R. F. Weiss, 1985, Chemistry
976   of submarine hydrothermal solutions at 21 °N, East Pacific Rise: Geochimica et Cosmochimica
977   Acta, v. 49, no. 11, p. 2197–2220, doi:10.1016/0016-7037(85)90222-4.

978   Von Damm, K. L., C. M. Parker, M. D. Lilley, D. A. Clague, R. A. Zierenberg, E. J. Olson, and J. S.
979   McClain, 2006, Chemistry of vent fluids and its implications for subsurface conditions at Sea

980   Cliff hydrothermal field, Gorda Ridge: CHEMISTRY OF VENT FLUIDS: Geochemistry,
981   Geophysics, Geosystems, v. 7, no. 5, p. n/a-n/a, doi:10.1029/2005GC001034.

982 Wallace, P. J., T. Plank, M. Edmonds, and E. H. Hauri, 2015, Volatiles in Magmas, *in* The Encyclopedia
983   of Volcanoes: Elsevier, p. 163–183, doi:10.1016/B978-0-12-385938-9.00007-9.

984 Wilson, D. S., 1993, Confidence intervals for motion and deformation of the Juan de Fuca Plate: Journal
985   of Geophysical Research, v. 98, no. B9, p. 16053, doi:10.1029/93JB01227.

986 Wolery, T. J., 2010, EQ3/6 A Software Package for Geochemical Modeling: Lawrence Livermore
987   National Lab.(LLNL), Livermore, CA (United States).

988 Zierenberg, R. A., P. Schiffman, I. R. Jonasson, R. Tosdal, W. Pickthorn, and J. McClain, 1995,
989   Alteration of basalt hyaloclastite at the off-axis Sea Cliff hydrothermal field, Gorda Ridge:
990   Chemical Geology, v. 126, no. 2, p. 77–99, doi:10.1016/0009-2541(95)00111-2.

991

Sea-based team:
Implementation of dive plan + onboard chemical analysis

Land-based team:
Data processing with modeling →
Result-informed design of dive plan

ROV *Hercules*

Hydrothermal chimney

Image credit: OET/Nautilus Live

Increasing mixing

Rift-valley wall

Model
A B C

Model
A B C

Seawater

Step 1

Step 2

Temp. max.
(50-400°C)

Gas input
(CO_2, SO_2, H_2O)